

PHYSICS-INFORMED CRYSTAL PLASTICITY MODELING
FOR BODY-CENTERED-CUBIC METALS

By

Cathy (Ruxin Zhang) Bing

A DISSERTATION

Submitted to
Michigan State University
in partial fulfillment of the requirements
for the degree of

Physics—Doctor of Philosophy

2025

ABSTRACT

Understanding and modeling the plastic deformation of body-centered cubic (BCC) metals remains a central challenge in materials science due to the complex nature of BCC dislocation mechanisms. This dissertation applied a physics-informed approach in crystal plasticity modeling for BCC metals by addressing three core challenges: experimental-model calibration consistency, dislocation mobility formulation, and constitutive model completeness.

The first study investigates the reliability of using surface-based measurements for calibrating crystal plasticity models for bulk materials. Plastic deformation behavior is most conveniently assessed by characterization on a surface, but whether such observations are representative of bulk properties is uncertain. Motivated by reported inconsistencies in slip resistance probed at different depths, we investigated (i) whether the average slip family activity is affected by the presence of a surface and (ii) how the kinematic nature of available slip families influences a potential surface effect. The slip family activity as a function of distance from the surface was extracted from full-field crystal plasticity simulations of random polycrystalline hexagonal close-packed (HCP) and BCC metals as examples of mixed in contrast to universally-high numbers of slip systems per family. Under certain conditions, a deviation from bulk slip activity is observed up to about two grains from the surface. For the easiest (least slip-resistant) family, a surface effect of decreasing activity with depth emerges if the number of slip systems falls below about six. For harder families, slip activity always increases with depth. These phenomena are explained on the basis of varying constraints with depth in connection with the kinematic properties of slip families in the material.

The second study develops a generalized mobility law for dislocations in BCC metals based on the kink-pair mechanism. Dislocation mobility laws are key to dislocation-density-based crystal plasticity modeling. For dislocations following the kink-pair mechanism, however, existing formulations are often restricted to specific regimes due to the complex interplay between stochastic kink-pair nucleation and lateral kink migration. In this study, the average dislocation velocity under the kink-pair mechanism is formulated as a function of five variables: kink-pair nucleation rate, kink migration velocity, dislocation segment length, critical kink-pair width, and kink height.

Through probabilistic cellular automaton simulations, the propagation of conceptual dislocation segments is tracked across a wide range of conditions, and their average velocities are systematically fit using a hyperbolic tangent function. The resulting full-range formulation remains valid for arbitrary combinations of the five variables, and is therefore compatible with a wide variety of underlying kinetic laws. Comparisons with established models demonstrate the consistency and robustness of the new formulation, making it suitable for diverse material systems in which the kink-pair mechanism governs dislocation motion.

The third study presents a comprehensive constitutive model that explicitly differentiates between edge and screw dislocation populations. The model incorporates distinct mobility laws for each dislocation character, reflecting the fundamental differences in their motion mechanisms: screw dislocations move via a thermally activated kink-pair process, while edge dislocations glide more readily with lower thermal sensitivity. In addition, separate density evolution laws are developed for edge and screw dislocations, accounting for processes such as dipole formation, annihilation, and interaction-driven hardening. The model includes physically motivated mechanisms such as cross-slip for screws and climb for edges, which further enrich the fidelity of dislocation evolution under complex loading conditions. Implemented within the DAMASK simulation platform, the model is built with a modular structure that allows each mechanism to be activated or deactivated independently. This design enables systematic investigations into the role and interplay of individual features, supporting both predictive simulations and fundamental studies of BCC deformation behavior.

Collectively, this work lays the foundation for a robust and extensible framework for modeling the plastic behavior of BCC metals. It provides a deeper understanding of the microstructural mechanisms governing deformation and offers practical tools for predictive simulation of advanced metal systems under varied thermomechanical conditions.

ACKNOWLEDGEMENTS

I would like to first thank my advisor, Dr. Philip Eisenlohr, for his continued support throughout my PhD journey and being a wise guider to a young researcher. I have learned a great deal from him beyond the subject of crystals, including how to calmly navigate uncertainty, how to plan strategically in all circumstances, and how to communicate ideas to different audiences. He has an ability to always radiate positivity, and I deeply admire how he creates an uplifting atmosphere wherever he goes. I hope to carry forward the lessons I have learned from him, and to grow into someone who brings that same sense of light and support to others.

I also want to express my gratitude for the good fortune of having Dr. Thomas Bieler as a mentor, who is always kind, caring, and approachable. I still remember an afternoon at my first TMS conference when I moved between three different sessions, and as I enter each one, the speaker was referring to a different work by him on titanium plasticity. That moment left a strong impression on me—it was when I realized that my career goal would be to become the kind of expert in a field I love, and to contribute to it throughout my life, as he has. Now entering this new chapter in retirement, I sincerely hope he enjoys it fully and happily—although he still attends the weekly group meeting.

I am grateful for the valuable guidance and support from my committee members Dr. Kendall Mahn, Dr. Carlo Piermarocchi, and Dr. Remco Zegers. They consistently helped ensure my doctoral work stayed on a meaningful path and prepared me well for my future career.

I am also deeply thankful to Dr. Martin Crimp, Dr. Carl Boehlert, and other members of the MSU Metals Group for the insightful comments and feedback that led to significant improvements in the scope and clarity of my research.

My appreciation also goes to Dr. Peter Lee, Dr. Eric Taleff, and other collaborators involved in the project on superconducting radiofrequency (SRF) niobium cavities, for the thought-provoking discussions and warm encouragement throughout the last few years.

Special thanks go to the High-Performance Computing Center (HPCC) at the Institute for Cyber-Enabled Research (ICER) and the Division of Engineering Computing Services (DECS),

for providing the computational resources essential to my studies.

Studies consisting this dissertation were supported by the U.S. Department of Energy, Office of Science, Office of Basic Energy Sciences, under award numbers DESC0001525 and DESC0009960.

TABLE OF CONTENTS

CHAPTER 1	INTRODUCTION	1
1.1	Dislocation-mediated plasticity in metals	1
1.2	Crystal plasticity finite element modeling	3
1.3	Constitutive laws	7
1.4	Challenges of Modeling BCC Metals	8
1.5	Structure of the Dissertation	11
CHAPTER 2	SURFACE EFFECT ON DISLOCATION SLIP ACTIVITY	12
2.1	Motivation	12
2.2	Methods	15
2.3	Results and Discussion	21
2.4	Conclusions	30
CHAPTER 3	A GENERAL MOBILITY LAW FOR BCC SCREW DISLOCATIONS .	32
3.1	Introduction	32
3.2	Methods	35
3.3	Results	37
3.4	Discussion	40
3.5	Conclusions	46
3.6	Data Availability	46
CHAPTER 4	A COMPREHENSIVE CONSTITUTIVE MODEL FOR BCC METALS	47
4.1	Introduction	47
4.2	Constitutive model	48
4.3	Implementation	57
4.4	Summary	58
CHAPTER 5	CONCLUSIONS AND FUTURE WORK	60
BIBLIOGRAPHY		61

CHAPTER 1

INTRODUCTION

1.1 Dislocation-mediated plasticity in metals

Dislocations are line defects in crystalline materials that play a central role in plastic deformation. Figure 1.1 shows a schematic representation of a dislocation line (AB, dashed red line), around which the crystal lattice is distorted. The magnitude and direction of this distortion is described by the Burgers vector \mathbf{b} , shown as red arrows. Depending on the relative orientation between the dislocation line and its Burgers vector, dislocations are classified as screw (parallel), edge (perpendicular), or mixed (intermediate angles). In the illustrated example, the dislocation is a pure screw at A, pure edge at B, and mixed in between where there is curvature.

In crystalline metals, plastic deformation proceeds predominantly through the motion of dislocations, rather than by uniform shear of atomic planes. For an ideal, defect-free crystal, the critical stress required to initiate plastic deformation [30] is several orders of magnitude higher than what is observed experimentally for normal metals. This discrepancy led to the theory of dislocation-mediated plasticity in metals [53, 84, 62].

In Fig. 1.1, the lattice distortion expands through the motion of dislocation line AB, a process known as slip. From this perspective, a dislocation can also be defined as the boundary of a slipped area. The crystallographic plane (ABC) along which the dislocation line moves is termed as the slip plane, and the slip direction is defined by the Burgers vector. Together, the slip plane and slip direction constitute a slip system. Figure 1.2 illustrate the common slip systems (grouped into slip families based on symmetry) in the hexagonal close-packed (HCP) lattice. The critical stress required to initiate plastic deformation in real metals with defects is thus translated to the stress required to move dislocations in a slip system, *i.e.* the slip resistance, which is much lower than the stress to shear an atomic plane uniformly.

The connection between dislocation motion and continuum plasticity was established by the Orowan equation [53]:

$$\dot{\gamma} = \rho b \bar{v}, \quad (1.1)$$

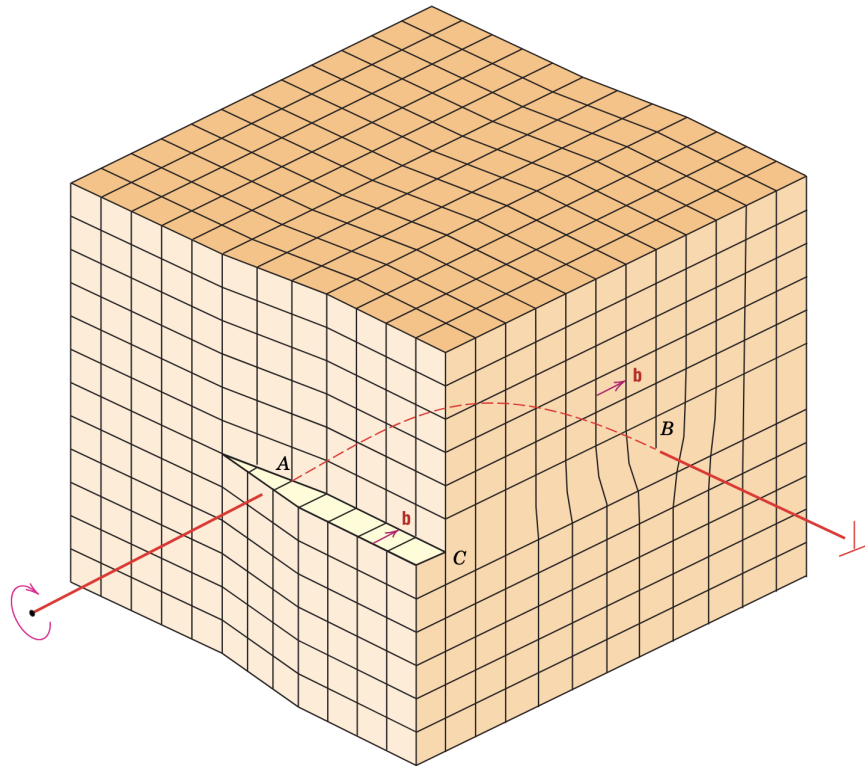


Figure 1.1 Schematic of a dislocation line (dashed red) exhibiting screw, mixed, and edge character from A to B [17]. The Burgers vector \mathbf{b} , shown in red arrows, remains constant along the dislocation.

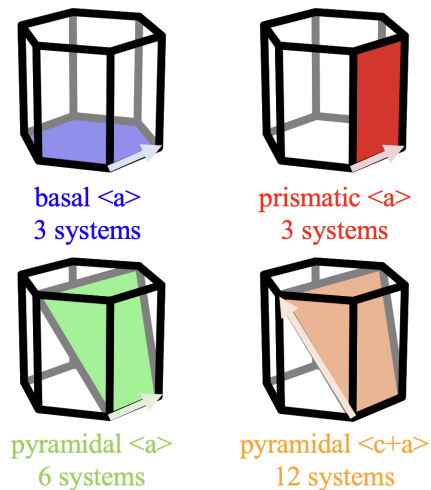


Figure 1.2 Four common slip families in the hexagonal close-packed (HCP) lattice, where slip systems that are crystallographically equivalent are grouped together. The slip plane in each slip family is shaded, and the slip direction is indicated by an arrow.

where $\dot{\gamma}$ is the plastic shear strain rate, ρ is the dislocation density, b is the magnitude of the Burgers vector, and \bar{v} is the average velocity of dislocations. Understanding of dislocation theory and quantifying related physical quantities (*e.g.*, the slip resistance) are essential for modeling crystal plasticity in a physically meaningful and reliable manner.

1.2 Crystal plasticity finite element modeling

1.2.1 Background

Crystal plasticity modeling is a mesoscale, continuum-level computational approach used to predict the plastic behavior of crystalline materials by explicitly accounting for crystallographic anisotropy and the slip of dislocations as the dominant deformation mechanism [61, 89]. Early models of crystal plasticity [70, 85] relied on simplified boundary conditions, assuming uniform stress or strain across the grains (crystals in a polycrystalline material). Although these approaches offered initial insights, their homogenizing assumptions limit the ability to resolve microscale phenomena such as texture evolution, local field fluctuations, and strain localization.

To overcome these limitations, the crystal plasticity finite element method (CPFEM) was developed by integrating crystal plasticity formulations with the finite element method [59, 67]. This extension enables the resolution of micromechanical interactions within and across grains under complex internal and external boundary conditions (see Fig. 1.3). CPFEM is thus a powerful tool for implementing comprehensive theories of plasticity that incorporate underlying deformation mechanisms and support the development of physically based predictive models for advanced engineering applications [99, 3, 102].

A CPFEM framework that is closely related to this dissertation is the Düsseldorf Advanced Material Simulation Toolkit (DAMASK) [68], an open-source, unified, multi-physics crystal plasticity simulation package. DAMASK employs a numerically efficient spectral method to solve the mechanical boundary value problem of static equilibrium, offering both robustness and computational efficiency for complex simulations [72, 78].

In this dissertation, DAMASK is used in two studies: the investigation of surface effects on slip activity presented in Chapter 2, and the development of a comprehensive dislocation-density-based

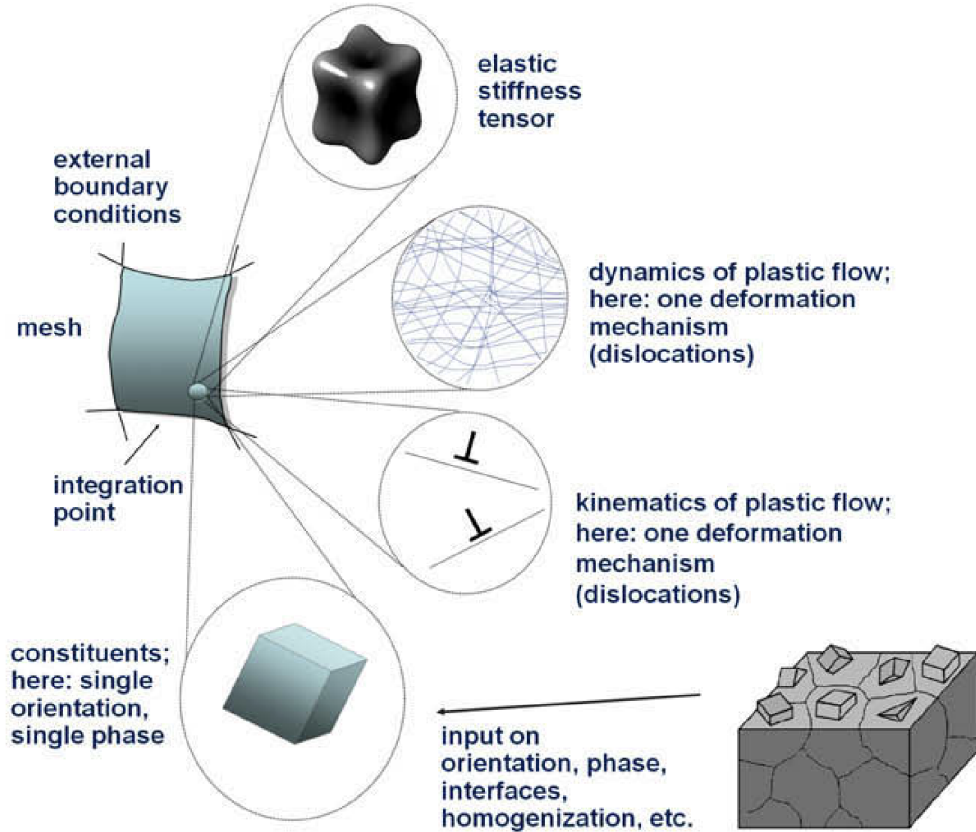


Figure 1.3 Schematic presentation of the conceptual ingredients in crystal plasticity finite element simulations [67].

model described Chapter 4, for which a dedicated module was developed and integrated into the DAMASK framework.

1.2.2 Finite strain framework

CPFEM is typically formulated within a finite strain framework to account for the large deformations experienced in plastically deforming crystals. This section summarizes the formulation implemented in DAMASK [68], which underlies the modeling work in both Chapter 2 and Chapter 4. Additional background and theoretical context are drawn from Roters et al. [69].

Consider an infinite number material points in a deformable body or continuum. As illustrated in Fig. 1.4, the body transforms from the undeformed (reference) configuration \mathcal{B}_0 into the deformed (current) state \mathcal{B} . The total deformation gradient is given by

$$\mathbf{F} = \frac{\partial \mathbf{y}}{\partial \mathbf{x}}, \quad (1.2)$$

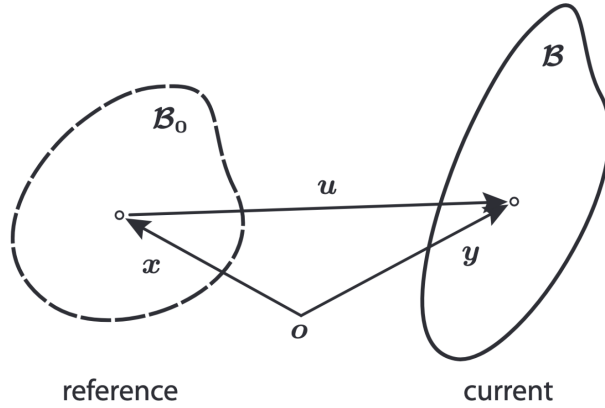


Figure 1.4 Deformable body occupying region \mathcal{B}_0 in the reference configuration and region \mathcal{B} in the current configuration [69]. The positions of material points are denoted by \mathbf{x} and \mathbf{y} in both configurations, respectively.

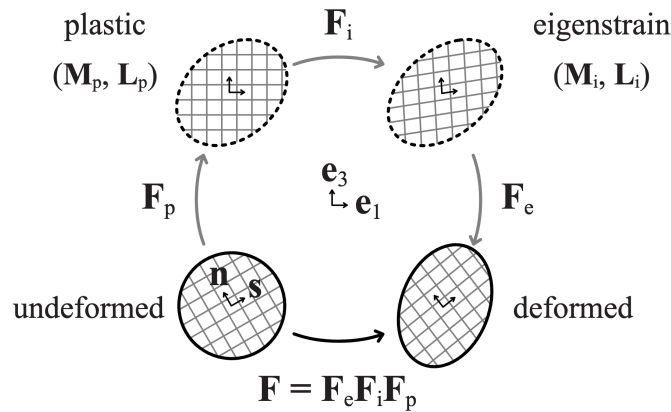


Figure 1.5 Illustration of the intermediate configurations resulting from the multiplicative decomposition of the deformation gradient [68].

where \mathbf{x} and \mathbf{y} are position vectors of material points in the undeformed and deformed configurations, respectively. The deformation gradient undergoes a multiplicative decomposition:

$$\mathbf{F} = \mathbf{F}_e \mathbf{F}_i \mathbf{F}_p, \quad (1.3)$$

where the undeformed configuration is mapped to the deformed configuration in three steps (see Fig. 1.5):

1. The inelastic, lattice-preserving \mathbf{F}_p maps to the plastic configuration, which comprises a rotation as well as the flow of material;

2. The inelastic, lattice-distorting \mathbf{F}_i accommodate stress-free strains (eigenstrains), such as thermal expansion or crack opening [79], mapping further to the intermediate configuration;
3. The elastic deformation gradient \mathbf{F}_e maps from the inelastic to the deformed configuration, corresponding to elastic stretching of the lattice.

Classical multiplicative decomposition can be made up by $\mathbf{F} = \mathbf{F}_e \mathbf{F}_p$, which is termed as elastoplastic decomposition. The consideration of \mathbf{F}_i is beneficial when stress-free strains are involved. For example, when mimicking the effect of a surface through the introduction of a slice of soft, dilatational material, as further demonstrated in Chapter 2.

The two inelastic deformation gradients evolve at rates

$$\dot{\mathbf{F}}_p = \mathbf{L}_p \mathbf{F}_p, \quad (1.4a)$$

$$\dot{\mathbf{F}}_i = \mathbf{L}_i \mathbf{F}_i, \quad (1.4b)$$

governed by the velocity gradients \mathbf{L}_p and \mathbf{L}_i that are driven by the Mandel stresses

$$\mathbf{M}_p = \mathbf{F}_i^T \mathbf{F}_i \mathbf{S}, \quad (1.5a)$$

$$\mathbf{M}_i = \det\{\mathbf{F}_i^{-1}\} \mathbf{F}_i \mathbf{S} \mathbf{F}_i^T, \quad (1.5b)$$

where both Mandel stresses are mappings of the second Piola–Kirchhoff stress

$$\mathbf{S} = \mathbb{C} : \frac{1}{2} \mathbf{F}_i^T \left(\mathbf{F}_e^T \mathbf{F}_e - \mathbf{I} \right) \mathbf{F}_i, \quad (1.6)$$

which follows Hooke's law, and \mathbb{C} is the fourth-order elastic tensor.

The plastic velocity gradient \mathbf{L}_p (see Eq. (1.4a)) results from deformation slip occurring across all considered slip systems, indexed by α . It is calculated by:

$$\mathbf{L}_p = \dot{\gamma}^\alpha \mathbf{m}^\alpha \otimes \mathbf{n}^\alpha, \quad (1.7)$$

where $\dot{\gamma}^\alpha$ is the shear rate on slip system α , \mathbf{m}^α is the unit vector along the slip direction, and \mathbf{n}^α is the unit vector normal to the slip plane (implicit summation over repeated indices). Additional

contributions to L_p beyond slip, such as twinning or phase transformations, can also be modeled but are not considered in this dissertation.

This kinematic framework provides the foundation for developing constitutive laws, which link the internal slip activity to external mechanical conditions.

1.3 Constitutive laws

Whereas the kinematic description (Eq. (1.7)) accounts for how slip on various crystallographic systems contributes to the overall deformation, it does not specify the extent of slip that occurs under given external stimuli. This essential link is provided by the constitutive laws, which provide material-specific relations between the mechanical conditions (*e.g.*, the applied stress state) and the resulting deformation slip. In the context of crystal plasticity, constitutive laws govern the evolution of shear rate on each slip system as a function of resolved shear stress (the projection of the applied stress onto a slip system), temperature, and internal microstructural variables. These laws are responsible for capturing key aspects of plastic behavior such as flow (plastic deformation), strain hardening, rate sensitivity, and thermal activation [69]. CPFEM offers a robust and flexible numerical framework to incorporate various constitutive laws at the level of individual slip systems.

Classical phenomenological constitutive laws [5, 66] employ empirical expressions fitted to experimental data to describe material behavior under various conditions. These approaches often involve specifying a flow rule and hardening law based on macroscopic behavior (such as power-law relationships), with internal state variables calibrated to match experimental observations. As a result, they can efficiently reproduce observed stress-strain behavior without requiring detailed knowledge of microstructural variables such as dislocation density or obstacle types. Despite their limited generalizability beyond the calibrated regime and lack of direct physical interpretability, they remain widely used due to the advantages in computational efficiency, ease of calibration, and numerical robustness. The study presented in Chapter 2 employed a phenomenological constitutive law to investigate the surface-biased slip activity, leveraging its practical performance and maturity.

In contrast, physics-informed constitutive laws aim to represent plastic deformation by explicitly incorporating the underlying mechanisms that govern the mesoscale physics. Dislocation-density-

based models [4, 3, 43] are a notable class of such approaches, wherein the motion and evolution of dislocations are directly coupled to the plastic response. These models typically include physical parameters for dislocation interactions, thermal activation mechanisms, and slip-system-specific kinetics, providing a more interpretable and extensible foundation across materials and conditions. The comprehensive model introduced in Chapter 4 exemplifies this strategy: dislocation densities are categorized by character (edge vs. screw) and configuration (monopole vs. dipole), with distinct mobility and evolution laws describing each group.

Regardless of the specific formulation, constitutive laws require calibration against experimental data. For phenomenological models, this typically involves fitting model parameters to reproduce observed stress-strain responses, a process that may be highly sensitive to the chosen experimental setup and boundary conditions. In physics-based models, although certain parameters can be informed by theory or derived from lower-scale simulations, others still necessitate experimental input for calibration. A central challenge arises when essential quantities, such as the crystallographic distribution of initial dislocation content, are difficult to measure directly, resulting in significant uncertainty in the corresponding model predictions [56]. Furthermore, data obtained from surface-sensitive experimental techniques (*e.g.*, scanning or transmission electron microscopy) may not accurately reflect bulk behavior, potentially introducing systematic biases into model calibration, which is a limitation further investigated in Chapter 2.

1.4 Challenges of Modeling BCC Metals

Body-centered cubic (BCC) metals present unique challenges for plasticity modeling due to their distinctive dislocation behavior and lattice characteristics. Unlike face-centered cubic (FCC) metals, which exhibit relatively straightforward slip behavior, BCC metals follow more complex and temperature-sensitive mechanisms, especially for screw dislocations.

1.4.1 Kink-pair mechanism

The kink-pair mechanism of dislocation motion [23] is illustrated in Fig. 1.6, which applies when the driving force is lower than the periodic energy barrier, which is termed as Peierls stress [58], and thermal activation is thus necessary for the propagation of dislocations. Dislocation segment

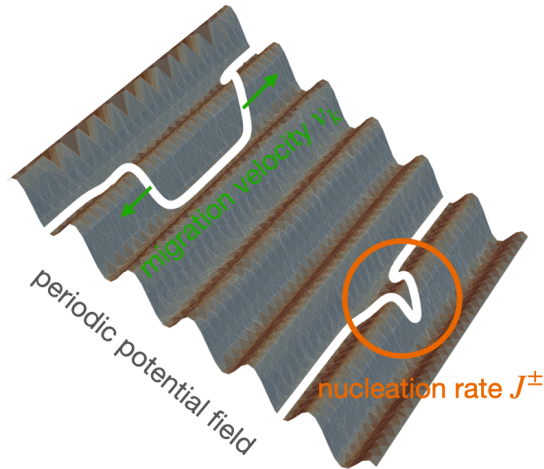


Figure 1.6 Illustration of the kink pair mechanism, where the dislocation lines (white) moves via thermally activated kink pairs and their subsequent lateral migration to opposite directions. Adapted from Fitzgerald [28].

(white lines) lying in a Peierls valley will have a chance to partially transition over the energy barrier into the neighboring Peierls valley by nucleating a pair of kinks (vertical steps), which is aided by thermal fluctuation. Both forward (positive) and backward (negative) kink-pair nucleation are possible, but are biased by an acting shear stress such that the positive kink-pair nucleation rate will always exceed the negative one. A kink pair that is too narrow is considered unstable, *i.e.* immediately collapses again, because the increase in dislocation line energy outweighs the plastic work and thermal energy. Under an acting shear stress, the lateral migration of kinks will collapse any negative kink pairs, whereas positive kink pairs expand and result in the overall forward motion of the dislocation.

The ratio of Peierls stress to the shear modulus for BCC screw dislocations is typically two magnitudes higher than that for edge dislocations [76, 47, 63]. Therefore, the motion of screw dislocations in BCC metals is well acknowledged to follow the kink-pair mechanism [75, 25, 96, 46], and the velocity of screw dislocation is much more limited compared to edges. The mobility of screw dislocations then becomes the rate-limiting process that dominates the plastic strain rate of BCC metals.

Numerous studies [31, 18, 74, 13] have introduced mobility laws that account for the kink-pair mechanism and its temperature dependence in order to accurately capture the plastic response

of BCC metals. However, due to the stochastic nature of thermal fluctuation and the complex nucleation-migration interplay, a general formulation for the average advancing velocity following the kink-pair mechanism is so far precluded, which is addressed in Chapter 3.

1.4.2 Non-planar core structure and cross-slip mechanism

A major reason for the high Peierls stress for screw dislocations in BCC metals is their non-planar core structure. Unlike BCC edge dislocations or FCC dislocations that are generally centered on a single crystallographic slip plane, BCC screws has a non-planar, spread-out core. Atomistic simulations have shown that the screw dislocation core in BCC metals does not lie neatly in one slip plane but spreads symmetrically into multiple adjacent slip planes that intersect along the dislocation line [88, 24, 87, 92].

The non-planar core enables a high propensity for cross-slip, a mechanism in which a screw dislocation switches its slip plane without requiring a substantial energy barrier. Unlike FCC metals, where cross-slip is possible but requires an additional activation stress and is less frequent, BCC screw dislocations are frequently observed to undergo repeated cross-slip events [27]. As a result, the slip traces they produce on the material surface often appear wavy or non-crystallographic, rather than aligned with a single slip plane. This easy cross-slip behavior provides several mechanical advantages: it allows screw dislocations to bypass obstacles, access alternate slip systems, and contribute to strain hardening and ductility by enabling more complex deformation paths.

However, these same features also introduce modeling and characterization challenges. The delocalized core complicates the definition of a unique slip plane for each screw dislocation, making it difficult to infer active deformation modes from experimental observations alone. In simulation frameworks such as CPFEM, conventional assumptions that tie each slip system to a fixed crystallographic plane may no longer be valid. Furthermore, the frequent cross-slip introduces orientation-dependent and stress-path-dependent responses that violate the assumptions of Schmid's law [73], requiring more sophisticated constitutive descriptions that incorporate non-Schmid effects [32].

The modeling work in Chapter 4 explicitly take into account the non-planar core structure

and cross-slip mechanism, as well as the kink-pair mechanism. The constitutive model developed in Chapter 4 explicitly addresses these complexities. A dedicated framework is introduced to separately account for the behavior of screw and edge dislocations, including the non-planar spreading of screw cores and their probability of cross-slip. These features are essential for capturing the distinctive plasticity mechanisms observed in BCC metals.

1.5 Structure of the Dissertation

This dissertation contains three studies, each addressing a specific aspect of the physics-based crystal plasticity modeling for BCC metals.

Chapter 2 investigates the validity of using surface-based measurements for calibrating crystal plasticity models for bulk materials, and discussed the underlying mechanism of the slip activity biased by surfaces.

Chapter 3 develops a general, full-range dislocation mobility law framework based on the kink-pair mechanism that captures the thermally activated motion of dislocations across a broad range of stress and temperature conditions, providing a foundation for more physically accurate modeling of BCC plasticity.

Chapter 4 introduces a comprehensive constitutive model for BCC metals. The model accounts for distinct mobility and evolution laws among different characters and configurations of dislocations, and is implemented within the DAMASK framework for simulation.

Together, these studies combine practical evaluation of calibration techniques, mechanism-informed mobility laws, and the integration of dislocation physics into a unified constitutive framework for BCC metals.

CHAPTER 2

SURFACE EFFECT ON DISLOCATION SLIP ACTIVITY

This chapter is largely based on the study by Bing et al. [10], with adaptation for the purposes of this dissertation.

2.1 Motivation

The evolution of dislocation content in a plastically deforming grain of a polycrystalline material generally results from a complex interaction between dislocation activity on multiple slip systems. The evolving dislocation structure results in differing slip resistance¹ to further slip on each slip system. As such, probing the activity of any potential slip system and its associated resistance is a valuable tool to understand the evolution of structure and deformation resistance under load. Moreover, the quantification of slip activity and deformation resistance is essential to formulate and validate models of crystal plasticity. Such models, when applied to simulate the heterogeneity of deformation usually exhibited in polycrystalline materials, allow interrogation of, for instance, the (spatially rare) events that are at the root of material degradation and ultimate failure.

The task outlined above becomes even more complex for materials that have multiple slip families, such as hexagonal (HCP) or body-centered cubic (BCC) metals, *e. g.*, Ti and Mg, or Fe. Over the past few decades, several techniques have been developed to extract essential information for understanding heterogeneous plasticity. In the following, we briefly summarize the major progress achieved specifically for HCP metals as an exemplar of the challenges.

The most intuitive way is to exclusively activate one selected slip system by intentionally orienting a single crystal relative to the load, as done, for instance, by Williams et al. [94], and confirming the intended activity by surface slip trace observation. However, if some slip families are significantly harder (*e. g.* pyramidal $\langle c + a \rangle$ in HCP metals), an easier slip family might be activated sooner even when the targeted (harder) system is in the most favored orientation (has the highest Schmid factor), thus frustrating the independent probing of such hard families.

¹frequently termed critical resolved shear stress (CRSS), usually associated with yielding, and sensitive to alloy content and microstructural defects

Alternatively, knowledge can be gained from simulating nano-indentation into a single grain using a suitable constitutive model, and fitting its parameters (*e. g.* slip family resistances) to match the experimental response. Multiple features have been used as the basis for comparison between simulation and experiment, such as the load–displacement response and surface topography [98] or variation of hardness with crystallographic orientation [71]. Important challenges for this approach include the uniqueness of the identified parameter set [52] and the reproducibility of the measured response, caused, for instance, by the variability of initial defect content and uneven surface finish [12, 39, 9, 100].

Diffraction-based methods offer a means to directly measure the distortion of the unit cell that can be translated into the stress tensor, and are used with various deconvolution techniques to identify slip resistances. Baczmański et al. measured the evolution of lattice plane spacings with increasing plastic strain in Mg by Multireflection Grazing Incidence X-ray Diffraction (MGIXD) [7], which only probes the surface grains, and by neutron diffraction in bulk grains [6]. The results differed and were fitted with a self-consistent crystal plasticity homogenization model, *i. e.* embedding each of the simulated grains in an infinite material of their average strength. The slip family resistances required to match the measurements exhibited a larger difference among slip resistances (a wider spread) and a lower basal $\langle a \rangle$ resistance for the surface than the bulk [7, table 3], suggesting a systematic difference in deformation activity for different slip families between surface and bulk grains.

Furthermore, synchrotron-based high-energy X-ray diffraction microscopy with far-field detection (ff-HEDM) is able to measure the average deviatoric stress tensor and lattice orientation of most grains within an illuminated sample volume of typically 1 mm^3 at multiple strain levels before and after plastic yielding. From such data, the shear stress on every slip system in each grain was derived and the evolving maximum values per slip family were interpreted as the characteristic slip resistances, *e. g.*, [54, 55]. Similar to the concern raised above in the case of oriented single crystals, the highest apparent slip resistances might not correlate with actual activity on those slip systems, but be a (trivial) consequence of plastic flow carried by other (easier) slip systems, thus limiting

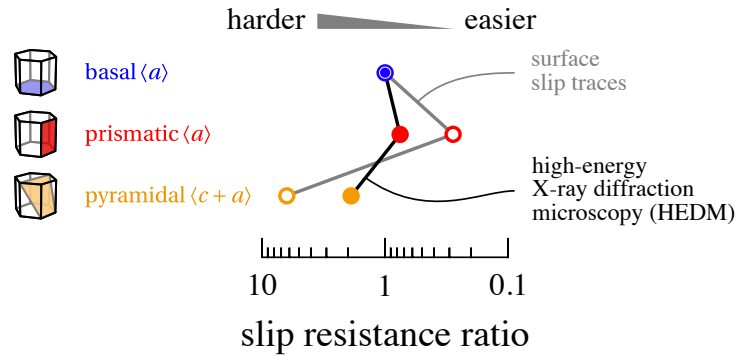


Figure 2.1 Slip resistance of (first-order) pyramidal $\langle c + a \rangle$ (orange) and prismatic $\langle a \rangle$ (red) relative to that of the basal $\langle a \rangle$ (blue) slip family as reported in two investigations sharing identical sample material of commercially pure Ti but differing depths of probed volume [90, 38] (open and filled circles, respectively). The surface slip resistances (open circles) exhibit a wider spread.

the overall maximum stress attained in such grains. One possibility to circumvent this uncertainty regarding actual slip activity is to compare the measured grain lattice orientation change to that expected for the assumed slip activity [55]. Another approach pursued by Wang et al. [90, 91] is based on the insight that dominant prismatic $\langle a \rangle$ slip causes a lattice rotation about the $\langle c \rangle$ -axis and dominant basal $\langle a \rangle$ slip about an axis perpendicular to $\langle c \rangle$. For grains that exhibited one of these two special rotations, the maximum resolved shear stress for the corresponding slip family was then averaged and interpreted as the respective slip resistance in commercially-pure Ti as sample material.

In contrast, a relatively inexpensive and straightforward approach to directly obtain the ratios between slip family resistances was proposed by Li et al. [38] based on the ratios of expected and observed frequencies of surface slip trace observations for each slip family and used, for instance, to investigate the influence of alloying elements on slip resistances in Mg [50].

In both cases where the same material was investigated with techniques that probe either (near-)surface or bulk locations, *i. e.* Mg [7, 19] and commercially-pure Ti [90, 38] (see also (Fig. 2.1), the spread in identified slip resistances turned out to be systematically wider when extracted close to the surface. As the idea of systematically different intrinsic slip resistances at different material depths seems unlikely, Chakraborty et al. [19] conjectured that a universal surface influence may exist because the mechanical constraint that opposes plastic deformation of a grain within a polycrystal

gradually decreases with proximity to the surface. The open question addressed in this work is when and how surfaces affect the slip family activity observed in a grain and whether the magnitude of this effect can be quantified and predicted such that inexpensive surface measurements can be used to extract bulk slip resistances.

To address the above question, we set up crystal plasticity simulations of thick polycrystalline film as well as bulk polycrystals as a reference. To investigate the influence of dissimilarity among slip families, HCP and BCC metals were used as examples for mixed in contrast to universally-high slip family multiplicity.² In HCP, basal $\langle a \rangle$, prismatic $\langle a \rangle$, and (first-order) pyramidal $\langle c + a \rangle$ were considered, whereas $\{110\}\langle 111 \rangle$ and $\{112\}\langle 111 \rangle$ slip families were included for BCC.

2.2 Methods

The simulations used the grid solver of the Düsseldorf Advanced Material Simulation Kit (DAMASK, [68]). The kinematic framework as the foundation of the following constitutive laws is introduced in Section 1.2.2.

2.2.1 Material constitutive description

The resolved stress on each slip system follows as the projection

$$\tau^\alpha = \mathbf{M}_p : (\mathbf{m}^\alpha \otimes \mathbf{n}^\alpha), \quad (2.1)$$

where \mathbf{M}_p is the Mandel stress, \mathbf{m}^α is the unit vector along the slip direction, and \mathbf{n}^α is the unit vector normal to the slip plane.

The rate of shear deformation is derived by

$$\dot{\gamma}^\alpha = \dot{\gamma}_0 \left| \frac{\tau^\alpha}{\xi^\alpha} \right|^n \text{sgn}(\tau^\alpha), \quad (2.2)$$

where $\dot{\gamma}_0$ is a reference shear rate and n denotes the stress exponent.

The resistance ξ^α to crystallographic slip along each slip system is modeled according to the phenomenological constitutive description introduced by Peirce et al. [59]. Following Brown et al. [15], the asymptotic evolution of each slip resistance from an initial value ξ_0^α to a saturation value

²The number of distinct slip systems in a family is called its ‘‘multiplicity’’.

Table 2.1 Constitutive parameters of exemplary HCP and BCC materials and the virtual air.

Property	Value			Unit
	HCP	BCC	Air	
c/a ratio	1.587	.	.	
ξ_0	various	various	0.03	MPa
ξ_∞/ξ_0	3	3	2	
h_0	0.2	1	10^{-3}	GPa
$h_{\alpha\beta}$	1	1 (coplanar) 1.4 (non-coplanar)	.	
$\dot{\gamma}_0$	10^{-3}	10^{-3}	10^{-3}	s^{-1}
n	20	20	5	
M	.	.	3	
a	2	2	2	

ξ_∞^α has contributions due to slip on all operating systems:

$$\xi_\infty^\alpha = h_0 \left| 1 - \frac{\xi^\alpha}{\xi_\infty^\alpha} \right|^a \operatorname{sgn} \left(1 - \frac{\xi^\alpha}{\xi_\infty^\alpha} \right) h_{\alpha\beta} |\dot{\gamma}^\beta|, \quad (2.3)$$

where h_0 is a reference hardening parameter, a is the hardening exponent, and $h_{\alpha\beta}$ characterizes the slip system interactions.

A similar constitutive description is used to describe the evolution of the eigenstrain gradient \mathbf{F}_i in the case of a “virtual air” layer introduced in Section 2.2.2 (see [68, 45] for details).

Parameters used in the simulations are listed in Table 2.1.

2.2.2 Geometry

To investigate how surfaces influence the slip family activity, polycrystalline structures with and without the presence of surfaces were constructed (Fig. 2.2) and labeled as “bulk” and “film”, respectively.

A periodic polycrystalline bulk structure (Fig. 2.2 left) contains $n_{\text{grain}} = 400$ randomly oriented grains resulting from a Voronoi tessellation of a random Poisson point distribution within a cubic volume discretized by $N = 96 \times 96 \times 96$ equidistant grid points. Reported values of slip family activity represent cumulative shear arising from each of the considered slip families averaged over the whole volume.

A freestanding polycrystalline film that is multiple grains thick results from inserting a layer of

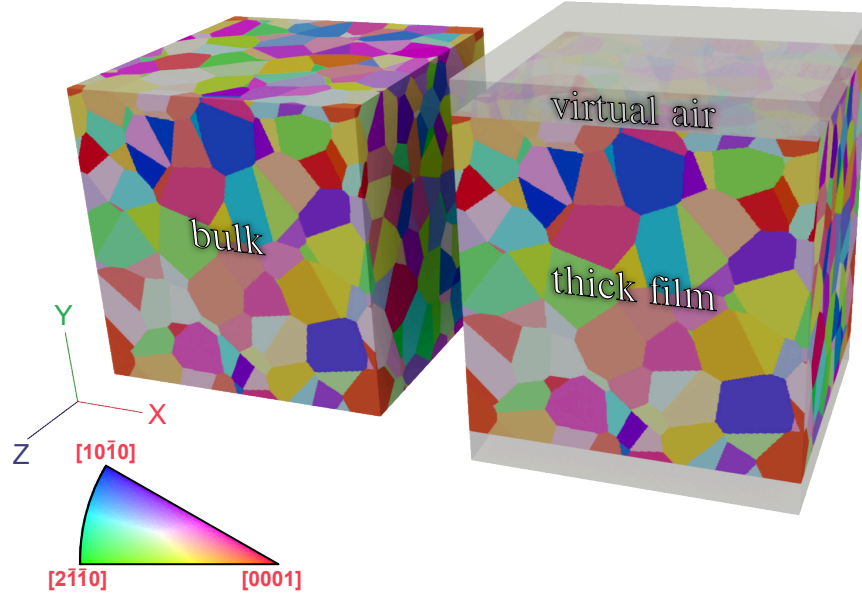


Figure 2.2 Exemplary unit cells of (left) periodic Voronoi tessellation with 400 grains mimicking a polycrystalline bulk structure, and (right) the same polycrystalline bulk structure but sandwiched by a layer of dilatational, soft, and compliant material (“virtual air”, translucent) to introduce two, essentially free, surfaces on top and bottom. Grain color reflects crystallographic direction along the loading axis x (with inverse pole figure coloring of hexagonal symmetry).

dilatational, low-strength, low-stiffness material (“virtual air”) into a periodic polycrystalline bulk structure to mechanically decouple the top and bottom faces (Fig. 2.2 right). Since the layer of virtual air can only exert a minuscule normal force (along y), both interfaces effectively act like free surfaces. In the case of the film structure, values of slip family activity are averaged per slice normal to the surface and reported as a function of distance to the nearest surface, *i.e.* as a depth profile.

Grid convergence was tested with three resolutions for the film structure as shown in Fig. 2.3 (left) while keeping the number of grid points discretizing the air layer along the surface normal constant. Since the chosen constitutive law is scale-independent, the coordinate system (specifically the distance to the surface) is normalized by the average grain diameter d_{grain}^3 as the only scale-determining quantity. Figure 2.3 (right) shows the slip activity depth profile observed for pyramidal $\langle c + a \rangle$, which is the worst converging one of all slip families in this example. Its slip activity is virtually identical between grid resolutions of 64^3 and 96^3 in the metal domain. Hence, $N = 96^3$

$${}^3N/n_{\text{grain}} = \frac{4\pi}{3} \left(\frac{d_{\text{grain}}}{2} \right)^3$$

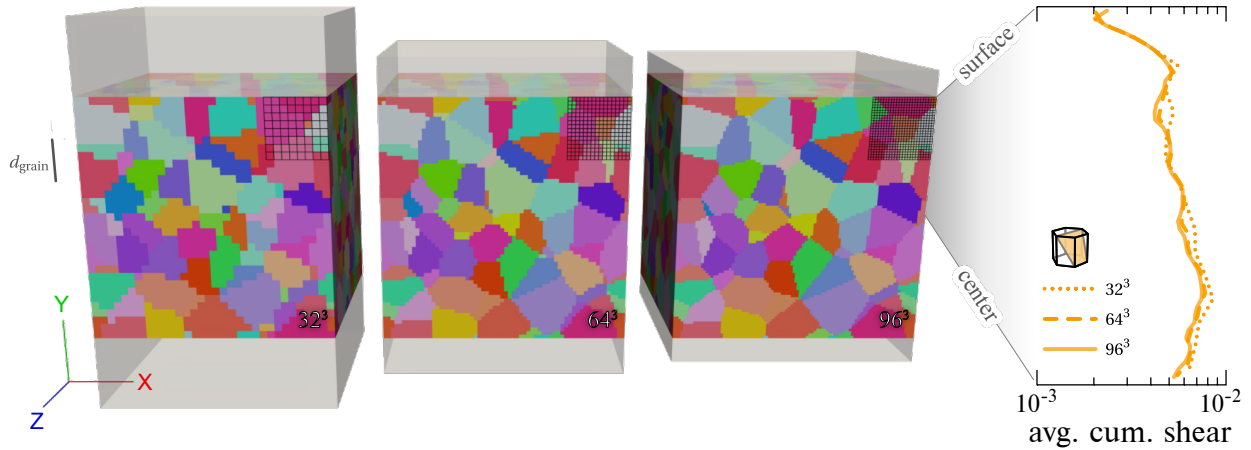


Figure 2.3 The same film structure discretized by $N = 32^3$, 64^3 , and 96^3 voxels within the metal domain, indicated by the black wireframe. The translucent air layer is $10 + 10$ voxels thick in all cases. The film center is about 3 grain diameters from the surface. The depth profile on the right shows the average cumulative pyramidal $\langle c + a \rangle$ shear in each slice after 5% strain along x for the three different grid resolutions.

was considered as a suitably converged resolution. Note that the first point from the surface in Fig. 2.3 (first layer of non-air voxels) is deviating from this overall converging behavior, most likely caused by the Gibbs phenomenon in response to the sudden property contrast across this interface.

2.2.3 Boundary conditions

Owing to the numerical solution strategy, all simulations obey periodic boundary conditions such that only volume-averaged stress or deformation values can be prescribed. Both the “bulk” and “film” structure are deformed along the x direction under mixed boundary conditions that are targeting a unidirectional stress response. Specifically, the volume-averaged deformation gradient

rate $\dot{\mathbf{F}}$ and work-conjugate first Piola–Kirchhoff stress \mathbf{P} values

$$\dot{\mathbf{F}}_{\text{bulk}} = \begin{bmatrix} 10^{-3} & 0 & 0 \\ 0 & \cdot & 0 \\ 0 & 0 & \cdot \end{bmatrix} \text{s}^{-1} \quad \text{and} \quad \mathbf{P}_{\text{bulk}} = \begin{bmatrix} \cdot & \cdot & \cdot \\ \cdot & 0 & \cdot \\ \cdot & \cdot & 0 \end{bmatrix} \text{Pa} \quad (2.4)$$

$$\dot{\mathbf{F}}_{\text{film}} = \begin{bmatrix} 10^{-3} & 0 & 0 \\ 0 & 0 & 0 \\ 0 & 0 & \cdot \end{bmatrix} \text{s}^{-1} \quad \text{and} \quad \mathbf{P}_{\text{film}} = \begin{bmatrix} \cdot & \cdot & \cdot \\ \cdot & \cdot & \cdot \\ \cdot & \cdot & 0 \end{bmatrix} \text{Pa} \quad (2.5)$$

were prescribed for a duration of 10 s and 50 s resulting in a final extension of 1 % and 5 %, respectively, as it is helpful to include the influence of work hardening in the scope of this work. A dot ‘·’ in Eqs. (2.4) and (2.5) indicates that the complementary condition is prescribed. Rather than adopting the bulk boundary condition for the film structure, the numerical convergence of the film improved notably (with an insignificant effect on the result) when preventing any extension along the surface normal, *i.e.* $\dot{F}_{yy} = 0$, such that any contraction of the crystalline volume along y is accommodated by a corresponding extension in the thickness of the (essentially stress-free) layer of virtual air.

2.2.4 Parametric study

To understand the effects of (i) crystal elasticity, (ii) differences in slip resistance per family, and (iii) multiplicity in easy and hard slip families on a potential surface effect, a parametric study along these three dimensions was performed.

2.2.4.1 Elasticity

To investigate the influence of elastic anisotropy, HCP was chosen as an example. Upon inspection of the elemental HCP metals, it turns out that their elastic anisotropy can be clustered into three groups as illustrated in Fig. 2.4. Table 2.2 summarizes the stiffness tensor components adopted in this study for HCP metals to represent these three distinct shapes (scaled to approximately equal overall magnitude) with some examples in each of the three groups, as well as for BCC metals and virtual air elasticity.



Figure 2.4 Directional stiffness in lattice frame coordinates illustrating each of the three representative instances of HCP elastic anisotropy listed in Table 2.2; from left to right and light to dark: “marshmallow”, “capsule”, and “spin”.

Table 2.2 Elastic stiffness tensor components of (isotropic) virtual air, three sample materials that span the anisotropy range of HCP metals, and an isotropic BCC material.

Material	Elastic stiffness tensor / GPa				
	C_{11}	C_{12}	C_{13}	C_{33}	C_{44}
virtual air	10^{-1}	10^{-3}	.	.	.
HCP					
marshmallow (Cd, Zn)	165	5	55	140	60
capsule (Be)	110	10	5	130	70
spin (Co, Mg, Zr)	165	90	60	190	40
BCC	270	110	.	.	80

2.2.4.2 Slip resistance

To discern whether the crystallography or the relative ease/difficulty of activation is the primary cause for a potential surface effect on the slip family activity, several choices of relative slip family resistances provide a comprehensive comparison (see left column of Fig. 2.5 and Fig. 2.7).

2.2.4.3 Slip family multiplicity

To understand whether the slip family multiplicity plays a role in a surface effect, the number of available slip systems in the pyramidal $\langle c + a \rangle$ family was artificially reduced to being equal to basal $\langle a \rangle$ and prismatic $\langle a \rangle$, *i.e.* from 12 to 3 for fixed slip resistances and elastic anisotropy (see left column of Fig. 2.6).

2.3 Results and Discussion

All parametric studies of film or bulk structures average 50 or 5 independent realizations, containing a total of $50 \times 400 = 20\,000$ or $5 \times 400 = 2000$ grains of random shape and orientation. Section 2.3.1 considers HCP metals as an example of lattices with mixed multiplicity, whereas BCC metals are investigated in Section 2.3.2 as example for universally high multiplicity. After summarizing the surface effect behavior in Section 2.3.3, corresponding mechanisms are discussed in Section 2.3.4.

2.3.1 HCP

Figure 2.5 displays the HCP slip family activity along the depth of the film structures (vertical curves) and in the bulk polycrystal (filled squares below bottom scale) up to 1 % and 5 % strain with their corresponding slip resistance ratios shown in the left column. Data is colored by slip family and the different shades indicate the three elastic anisotropy cases. Horizontal bars give the central 68 % of each slip family activity population. The vertical bar represents the average grain size d_{grain} , *i.e.*, the overall distance from the surface to the center of the film structure is about three grains.

2.3.1.1 Influence of elastic anisotropy

The influence of elastic anisotropy diminishes with increasing strain, as reflected by the differently shaded square symbols and associated depth profiles becoming overlaid in the right column of Fig. 2.5. The variability of slip activity (horizontal bars) with depth is only illustrated at three exemplary depths across the three elastic anisotropy instances as it turned out to not strongly depend on the specific anisotropy. Overall, the elastic anisotropy variations do not affect the shape of the depth profiles.

2.3.1.2 Bulk slip family activity

Naturally, the slip systems with the lowest slip resistance (rightmost in first column with reversed scale) values show the greatest activity. The (relative) spread in the slip family activity directly reflects the imposed slip resistance ratios. For instance, the larger ratios in row 8 (1:1:4) result in wider activity spread than the smaller ratios in row 7 (1:1:2). Thus, whenever the slip resistance

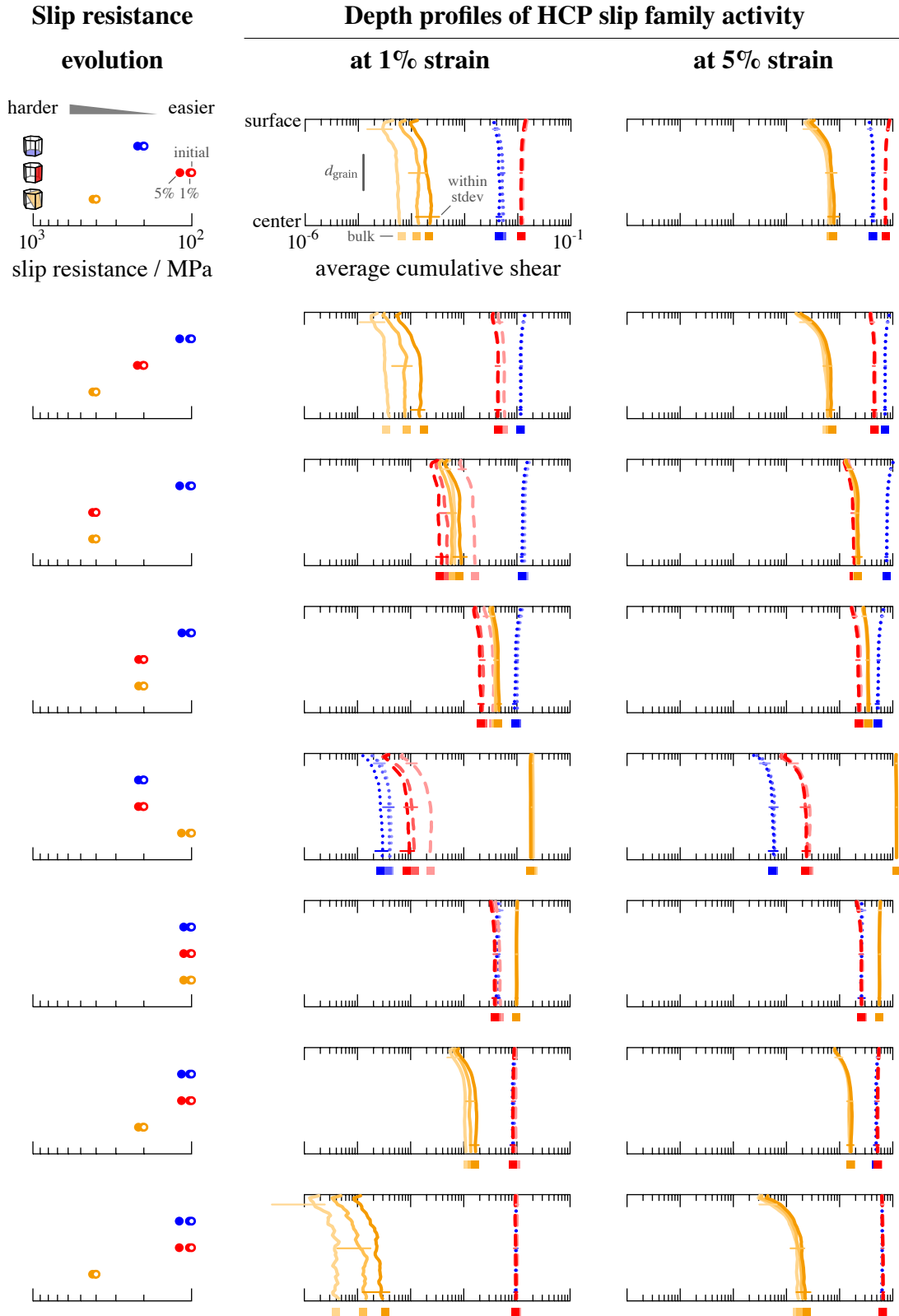


Figure 2.5 For eight cases of different slip resistance ratios in the left column, the right columns present the resulting depth profiles of slip family activity at two strain levels. Slip families are represented by different colors (and line styles) with shades reflecting the elastic anisotropy.

ratios narrow in response to strain hardening (filled circles compared to open ones), less favored slip families become relatively more active (shrinking distance between squares in column 3 compared to column 2).

2.3.1.3 Depth profiles of slip family activity

At a depth exceeding about $2 d_{\text{grain}}$, the activity in the film is essentially the same as that observed in the bulk, *i. e.* the value in the lower third of each curve is constant and equal to the corresponding square indicating bulk slip activity. In contrast, when approaching the surface (within $2 d_{\text{grain}}$), the slip activity of a film usually deviates from the bulk response. We note that the distance of about two average grain diameters beyond which a surface effect fades out is consistent with the results reported by Diehl et al. [22] in their investigation of “columnarity”, *i. e.*, how far away a change in grain structure is influencing the mechanical response in a bulk polycrystal.⁴

From the depth profiles presented in Fig. 2.5, two main observations can be made. The slip activity toward the surface

1. decreases for any slip family that is harder than the easiest
2. increases for the easiest slip family in case of basal $\langle a \rangle$ (row 2 (1:2:4), 3 (1:4:4), and 4 (1:2:2)) and prismatic $\langle a \rangle$ (row 1 (2:1:4)) but not for pyramidal $\langle c + a \rangle$ (row 5 (2:2:1)) or combined basal $\langle a \rangle$ and prismatic $\langle a \rangle$ (last three rows)

The latter observation suggests that the number of available slip systems in the easiest family (or a combination thereof) is a governing factor in the emergence of a surface effect.

2.3.1.4 Slip family multiplicity

To elucidate the influence of the number of available slip systems in the emergence of a surface effect for the easiest slip family, we select row 5 (2:2:1) of Fig. 2.5 as a test case and reduce the multiplicity of the (here easiest) pyramidal $\langle c + a \rangle$ slip family from 12 to 3.⁵ Figure 2.6 shows that this change results in a gradual increase of the activity of the two harder families (basal $\langle a \rangle$)

⁴We note the slight conceptual difference of “structural change” being the *removal* of grains beyond the surface in the present study in contrast to an *alteration* of those grains in ref. [22].

⁵The “capsule” elastic tensor from Table 2.2 was used.

Number of slip systems Depth profiles of HCP slip family activity at 5% strain

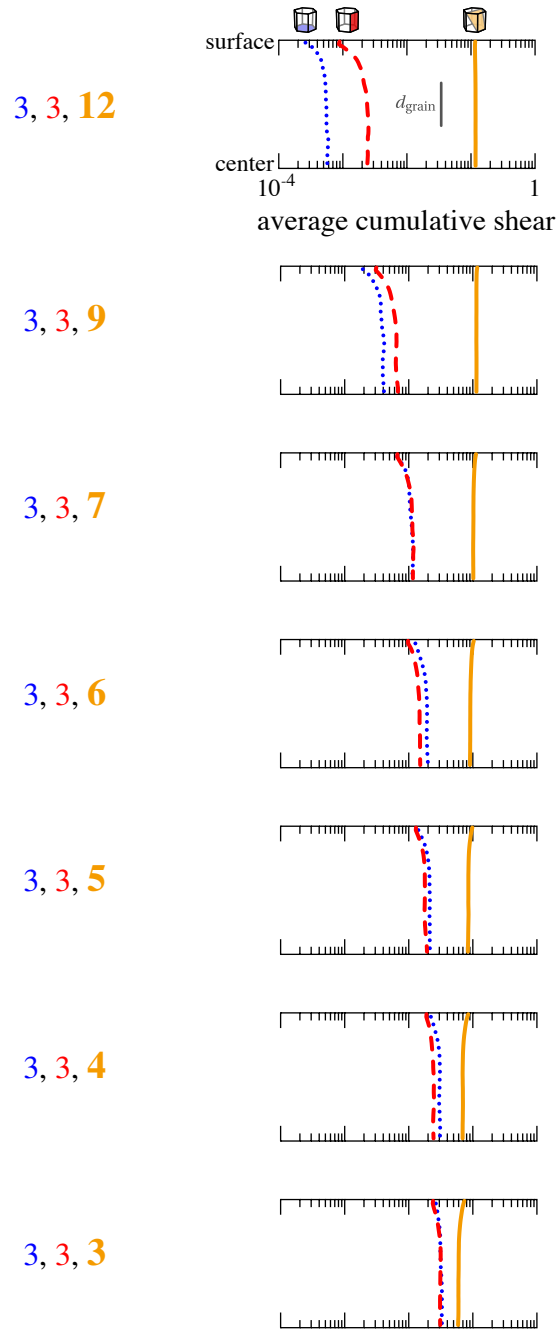


Figure 2.6 Slip activity of the three HCP slip families (basal $\langle a \rangle$, prismatic $\langle a \rangle$, pyramidal $\langle c + a \rangle$) as a function of distance from the surface for a fixed slip resistance ratio (same as row 5 (2:2:1) in Fig. 2.5) and elastic anisotropy (“capsule” in Table 2.2) but with a progressively reduced number of pyramidal $\langle c + a \rangle$ slip systems in the family (*i. e.* reduced multiplicity).

and prismatic $\langle a \rangle$) but does not qualitatively alter their surface effect, *i.e.*, the blue and red curves remain bent to the left. In contrast, the pyramidal $\langle c + a \rangle$ family develops an increasingly notable surface effect below a multiplicity of seven.

Such a surface effect is always present if the easiest slip family has low multiplicity. For instance, the surface effect of basal $\langle a \rangle$ (multiplicity of three) as the easiest family in rows 2 (1:2:4), 3 (1:4:4), and 4 (1:2:2) of Fig. 2.5 is very comparable to that of the reduced multiplicity pyramidal $\langle c + a \rangle$ in the bottom row of Fig. 2.6. Similarly, the combination of basal $\langle a \rangle$ and prismatic $\langle a \rangle$ as easiest families in row 7 (1:1:2) in Fig. 2.5 resembles the result for pyramidal $\langle c + a \rangle$ with the same (3+3) multiplicity of six in Fig. 2.6.

2.3.2 BCC

The combinations of multiplicity and slip resistance investigated so far suggest that in a situation of high multiplicity for soft as well as hard families, the surface effect is comparable to the results shown in rows 5 (2:2:1) and 7 (1:1:2) of Fig. 2.5. To test this hypothesis, we investigated an exemplary BCC material with two slip families, each having a multiplicity of twelve. Figure 2.7 follows the format of Fig. 2.5 and compares the slip family depth profiles after 5% strain across various slip resistance ratios between the $\{110\}$ (green) and $\{112\}$ (purple) slip families.

From top to bottom, the observed slip activity follows the changing ratios from strongly favoring $\{110\}$ to strongly favoring $\{112\}$. The decrease of activity with increasing relative slip resistance is asymmetric: $\{110\}$ slip (green curves top to bottom) shows a greater decrease than $\{112\}$ slip (purple curves bottom to top) at comparable slip resistances. This is most apparent in the middle row of Fig. 2.7, *i.e.* $\{112\}$ is more active than $\{110\}$ slip at equal slip resistance. We note in passing that for common BCC metals, the slip resistance of $\{110\}$ and $\{112\}$ is similar, perhaps within 10% of difference, *i.e.* close to the conditions shown in the middle three rows of Fig. 2.7. The difference in slip activity despite equally slip-resistant families (about 25% in the bulk of row 3 (1:2)) can be rationalized by the fact that for a random stress state, the chance that a $\{112\}$ slip system experiences the largest resolved shear stress is a few percent higher than for a $\{110\}$ slip system.

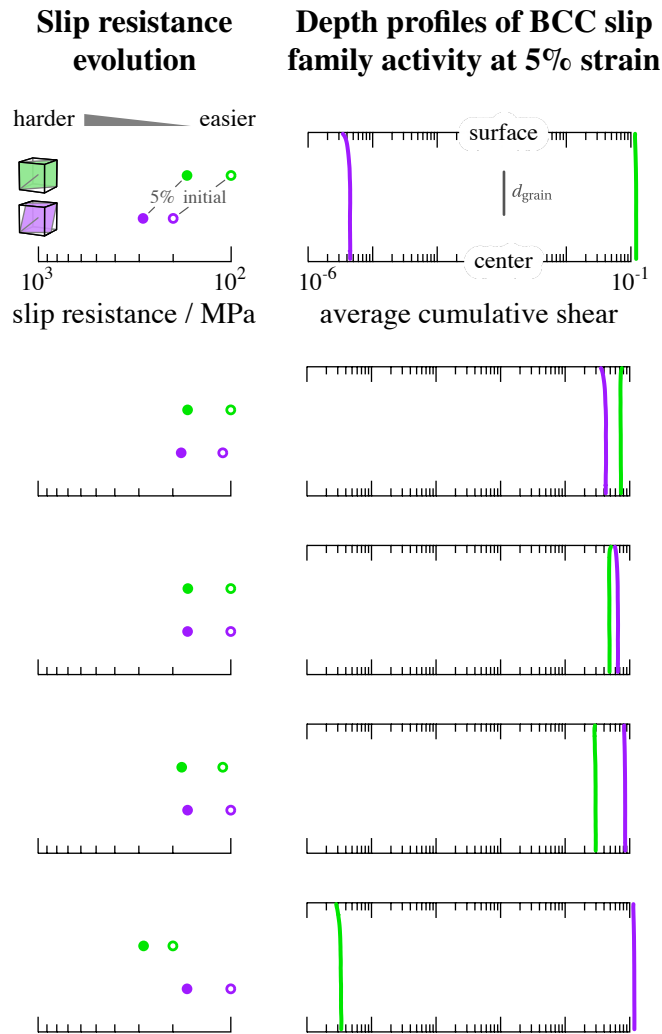


Figure 2.7 For five different slip resistance ratios in the left column, the resulting depth profiles of BCC slip family activity are presented in the right column after 5% strain. Closed circles in the left column correspond to the 95th percentile of slip resistances evolved after 5% strain from initial values (open circles). The vertical scale in the right column spans from the film surface to the center, about three grains deep. Variation across the central 68% of each slip family activity population is small and less than the curve widths. The slightly higher activity of $\{1\ 1\ 2\}$ compared to $\{1\ 1\ 0\}$ slip at equal slip resistance is connected to the slightly higher chance for a $\{1\ 1\ 2\}\langle 1\ 1\ 1\rangle$ slip system to have the largest Schmid factor.

Compared to what was observed for HCP metals under most conditions, the extent of surface effect in BCC cases is subtle to non-existent.

2.3.3 Types of surface effect manifestations

Overall, three distinct patterns a), b), and c) are observed for the surface effect on slip family activity:

- a) The activity of slip families that are harder than the easiest one is *decreased* near the surface relative to the interior, *e.g.* prismatic $\langle a \rangle$ and pyramidal $\langle c + a \rangle$ in row 2 (1:2:4) of Fig. 2.5, or basal $\langle a \rangle$ and prismatic $\langle a \rangle$ in row 5 (2:2:1) of the same figure.
- b) Conversely, the surface activity is *increased* for the easiest slip family provided its multiplicity is low, such as basal $\langle a \rangle$ in rows 2 (1:2:4) of Fig. 2.5, or pyramidal $\langle c + a \rangle$ in the bottom rows of Fig. 2.6.
- c) If the easiest slip family has considerable multiplicity, the surface effect on its activity is *virtually unnoticeable*, as demonstrated by the essentially straight curves of, for instance, pyramidal $\langle c + a \rangle$ in top rows of Fig. 2.6, combined basal $\langle a \rangle$ and prismatic $\langle a \rangle$ (featuring six slip systems in total) in row 7 (1:1:2) and 8 (1:1:4) of Fig. 2.5, or $\{1\ 1\ 2\}$ slip in row 4 (1.1:1) of Fig. 2.7.

Moreover, the surface effect intensifies with

1. larger slip resistance contrast, *e.g.* all three slip families in row 3 (1:4:4) of Fig. 2.5 show a larger curvature than in row 4 (1:2:2), a more drastic surface effect on pyramidal $\langle c + a \rangle$ slip activity is observed in row 8 (1:1:4) compared to row 7 (1:1:2), and for $\{1\ 1\ 0\}$ in row 5 (2:1) compared to row 4 (1.1:1) of Fig. 2.7;
2. larger multiplicity contrast, *e.g.*, with a slip resistance ratio of 2, Fig. 2.5 shows more pronounced surface effects than Fig. 2.7.

2.3.4 Mechanisms

Statistically, the best-aligned slip systems of the easiest slip family are activated first under loading, and the shape change caused by their activity generally leads to incompatibility with neighboring grains. In consequence, the stress state changes progressively favoring slip systems that help maintain compatibility. The overall compatibility constraints are naturally relaxed closer to the surface than further into the bulk. These ideas are at the core of the following explanations of the three different manifestations of the surface effect.

If the easiest slip family has numerous members (high multiplicity, typically more than six slip systems), chances are high that tighter compatibility requirements with increasing depth can be fulfilled by activating additional members of this (easiest) family. Therefore, if the observed slip activity is aggregated at the *family* level, there will be no substantial influence of changing compatibility constraints with depth on the overall activity of the easiest family, leading to pattern c), *i. e.*, no surface effect for the easiest family.

However, if the multiplicity of the easiest family is low, an increase in mechanical constraint, *i. e.* toward the interior, will decrease the chance to maintain compatibility by slip activity of that easiest family *alone*, resulting in decreasing activity of the easiest family with increasing depth as reflected in pattern b).

Because harder families are generally activated in response to mechanical constraint, their activity will decrease towards the surface, giving rise to pattern a), independent of whether or not softer families exhibit a surface effect.

When two or more low-multiplicity families share similar slip resistance values, this effectively increases the overall multiplicity of the resulting composite family and generally decreases a surface effect compared to its separate members. Examples are basal $\langle a \rangle$ and prismatic $\langle a \rangle$ in row 7 (1:1:2) and 8 (1:1:4) of Fig. 2.5, which, combined, act in a similar fashion as the sole softest pyramidal $\langle c + a \rangle$ in row 5 (2:2:1) of Fig. 2.5. Moreover, a gradual transition from three separate families into a combined higher-multiplicity family results when the slip resistance ratios approach one, as observed in the progression from row 2 (1:2:4) toward 4 (1:2:2) and 6 (1:1:1) of Fig. 2.5, which

strongly diminishes the surface effect. Conversely, an increasing slip resistance ratio between the easiest and harder slip families decreases the likelihood of activation for the harder families, resulting in a widened span of slip family activity, particularly at the surface (compare row 7 (1:1:2) and 8 (1:1:4) in Fig. 2.5).

Comparing the behavior between HCP and BCC (at slip resistance ratios of 2), the least and most active slip families differ by more than four orders of magnitude for BCC but no more than two orders of magnitude for HCP (*cf.* rows 1 (1:2) and 5 (2:1) in Fig. 2.7 and rows 4 (1:2:2), 5 (2:2:1), and 7 (1:1:2) in Fig. 2.5). This discrepancy is rooted in the similarity of the yield surfaces associated with the two BCC slip families in contrast to the dissimilarity of those associated with the basal $\langle a \rangle$, prismatic $\langle a \rangle$, and pyramidal $\langle c + a \rangle$ slip families [86]. Since the smallest rotation to align a $\{1\ 1\ 0\}$ slip system with the nearest $\{1\ 1\ 2\}$ system is only 30° , the two yield surfaces are very similar and, therefore, even a small difference in slip resistances between those two families strongly favors the easier family under virtually all possible deformation conditions. In contrast, a large misorientation of 64° and 79° between a pyramidal $\langle c + a \rangle$ slip system and its nearest basal $\langle a \rangle$ and prismatic $\langle a \rangle$ slip system, respectively, implies that basal $\langle a \rangle$ —and even more so prismatic $\langle a \rangle$ —offers kinematic degrees of freedom where pyramidal $\langle c + a \rangle$ is lacking, despite its high multiplicity of 12. This kinematic anisotropy of pyramidal $\langle c + a \rangle$ causes the pyramidal $\langle c + a \rangle$ yield surface to be relatively extended (harder to reach) in those directions where basal $\langle a \rangle$ and prismatic $\langle a \rangle$ are most facile. Consequently, a very large slip resistance of basal $\langle a \rangle$ and prismatic $\langle a \rangle$ relative to pyramidal $\langle c + a \rangle$ would be required to fully preclude their activity under deformation conditions unfavorable for pyramidal $\langle c + a \rangle$, *i. e.*, where the pyramidal $\langle c + a \rangle$ yield surface is extended. This requirement of relatively large slip resistance ratios explains why, despite pyramidal $\langle c + a \rangle$ being *the* easiest family in row 5 (2:2:1) and *one of* the easiest in row 6 (1:1:1) of Fig. 2.5, there is still appreciable activity of basal $\langle a \rangle$ and especially prismatic $\langle a \rangle$, since both contribute slip activity for deformation conditions that do not align well with pyramidal $\langle c + a \rangle$ kinematic degrees of freedom.

Another consequence of the similarity between the two BCC slip families, in contrast to the

dissimilar HCP families, is the lack of a large (relative) surface effect for the hardest family in BCC compared to a much more substantial effect in HCP (pyramidal $\langle c + a \rangle$ in row 8 (1:1:4) of Fig. 2.5). This is due to the shape of the yield surfaces spanned by each of the two BCC slip families being very similar, so any changes in the deformation boundary conditions experienced near the surface compared to the bulk will not substantially alter the ensuing slip activity, as demonstrated by the modest surface effects observable in Fig. 2.7 (particularly row 3 (1:2)).

2.4 Conclusions

Published slip resistance values of, for instance, magnesium and commercially pure titanium, determined through a variety of experimental means exhibit differences that suggest a systematic influence of the surface on the activity of hexagonal slip families. Crystal plasticity simulations of polycrystalline film and bulk structures were carried out to investigate the influence of a surface on the slip family activity in hexagonal close-packed (HCP) and body-centered cubic (BCC) materials. We could demonstrate that two main factors determine the strength of a surface effect, namely the contrast in slip family resistances (slip resistance ratios) and how similar the different slip families are (with similarity generally increasing with increasing multiplicity). Any variation in elastic anisotropy had no appreciable influence on the surface effect. Compared to the bulk interior, the activity of harder slip families always diminishes near a surface. The activity of the easiest slip family, especially when it has less than about six available slip systems, exhibits a notable increase in activity near the surface due to the relaxed constraints. Such a surface effect extends to a depth of approximately one to two average grain diameters, and it is amplified with increasing slip resistance ratios.

Based on the present results, given that pyramidal $\langle c + a \rangle$ slip is generally more difficult than basal $\langle a \rangle$ or prismatic $\langle a \rangle$ slip in HCP materials, a significant surface effect of pyramidal $\langle c + a \rangle$ should be anticipated. Specifically, if the sample dimension or slip resistance measurement methodology restricts the probed depth to less than about two average grain diameters, a significant overestimation of the slip resistance for the hard pyramidal $\langle c + a \rangle$ family is expected, along with an underestimation for the easiest family. The magnitude of this surface effect increases with the slip

resistance ratio between the hardest and softest families, and inversely with the multiplicity of the easiest family. For HCP metals, the shallower the probed depth, and the greater the ratio between hardest (pyramidal $\langle c + a \rangle$) and easiest (basal $\langle a \rangle$ or prismatic $\langle a \rangle$) slip resistance, the stronger the expected surface effect.

In contrast, combinations of high-multiplicity slip families do not exhibit a significant surface effect, as demonstrated using $\{1\ 1\ 0\}$ and $\{1\ 1\ 2\}$ slip families in BCC materials. The observed larger average activity of $\{1\ 1\ 2\}$ over $\{1\ 1\ 0\}$ slip for equal resistance and multiplicity is connected to their kinematic difference (twice as many $\{1\ 1\ 2\}$ than $\{1\ 1\ 0\}$ planes) that makes it slightly more likely to have the highest resolved shear stress on a $\{1\ 1\ 2\}$ slip system.

To sum up, this investigation reveals that interpretation of *statistical* slip behavior needs to be done carefully, as responses collected near a surface could differ from bulk locations. This is particularly relevant for materials featuring low-multiplicity slip families such as HCP, whereas BCC and FCC metals, in which all slip families have high multiplicity, are virtually unaffected.

Data availability

Scripts employed to generate the data that support the findings of this study are available at https://github.com/CathyBing/slip_surface_effect.

CHAPTER 3

A GENERAL MOBILITY LAW FOR BCC SCREW DISLOCATIONS

3.1 Introduction

The mobility law of dislocations is a critical component of dislocation-density-based crystal plasticity models, where the plastic strain rate depends on the average dislocation velocity [53]. Accurate modeling of dislocation mobility is essential for the prediction of reliable temperature- and time-dependent plastic responses. However, formulating a mobility law becomes particularly challenging for dislocations that move via complex mechanisms. For instance, in material systems with high Peierls stress [58], dislocation motion often follows the kink-pair mechanism [23], *i. e.*, a dislocation segment advances by the thermally activated nucleation of kink pairs and the subsequent lateral migration of both kinks in opposite directions. This mechanism is widely accepted to govern screw dislocation motion in body-centered cubic (BCC) metals [75, 25, 96, 46]. Due to the stochastic nature of thermal fluctuations, the complex interplay between kink-pair nucleation and kink migration has so far precluded a general analytical formulation of the average dislocation velocity under arbitrary conditions.

Despite the absence of a general solution, several mobility laws have been developed under simplifying assumptions tailored to specific regimes of the kink-pair mechanism. Since the kink-pair mechanism is commonly used to describe screw dislocation motion in BCC metals at low homologous temperatures, most existing models are constructed in the nucleation-limited regime, *i. e.*, under the assumption that only a single kink pair exists on a dislocation segment at a time. In this single-kink-pair regime, the dislocation velocity is a linear function of the kink-pair nucleation rate [51, 83, 16, 49, 1, 48, 28], with differences across models arising from how the nucleation rate is formulated. Another approach [18, 74] is to take the harmonic average of the kink-pair nucleation and migration speeds. Although this yields an intuitive blending of the two processes, the implicit presumption of only a single kink pair being active on the segment limits its validity to the rare-nucleation regime.

Some models are applicable beyond the nucleation-limited regime. Hirth and Lothe [31]

proposed an expression based on kink diffusion theory that captures both the single kink-pair and the multiple kink-pair regimes, and connected the two asymptotic solutions by harmonic averaging. More recently, Boleininger et al. [13] developed a statistical mechanics formulation that, although derived under the presumption of rare kink-pair nucleation rate, offers a limited extension beyond this regime.

Although many existing mobility models are developed under the assumption that only a single kink pair is active at a time, the kink-pair mechanism has been observed under much broader conditions that go beyond this regime. For example, a phase-field dislocation dynamics study by Jones et al. [33] showed that screw dislocations in niobium transition from single to overlapping kink-pair motion as temperature increases from 150 K to 400 K (homologous temperature 0.05 to 0.15), with a change in dislocation profile from straight to rugged, under an applied shear stress of 0.57 times the Peierls stress. This observation indicates that the single-kink-pair assumption breaks down even for relatively moderate temperature regimes of BCC metals.

Moreover, while the kink-pair mechanism is commonly associated with screw dislocations in BCC metals, it has also been reported for other scenarios. Molecular dynamics simulations [20, 97] suggest that edge dislocations in BCC metals may also propagate via the kink-pair mechanism, and nucleation dominates over lateral kink migration. In alloy systems, solute atoms can hinder kink migration, effectively shifting the rate-limiting process from nucleation to migration [101, 8]. These reports necessitate models that remain valid when kink migration becomes the bottleneck.

Finally, while blending limiting solutions (*e.g.*, using harmonic averages) may provide rough estimates, such approaches fail to accurately model the transitional regimes. Therefore, a dislocation velocity formulation that captures the full-range interplay between the nucleation and migration processes will extend the applicability of the kink-pair mechanism to broader contexts and result in more reliable predictions.

Despite the inherent stochasticity of kink-pair nucleation, the average dislocation velocity resulting from the kink-pair mechanism should, in principle, be expressible in a general and deterministic form. In other words, the average dislocation velocity \bar{v} should be representable as a

function of:

1. critical kink-pair width w at which a kink pair will not immediately collapse after nucleation,¹
2. segment length L of the propagating dislocation,
3. mean rates J^\pm of nucleating a kink pair of width w on a dislocation segment of length L causing positive/negative plastic work,
4. lateral migration velocity v_k of individual kinks,
5. distance h between two adjacent Peierls valleys.

Since \bar{v} is proportional to the kink height h , the formulation can be simplified as

$$\frac{\bar{v}}{h} = \bar{v} = F(J^+, J^-, v_k, L, w), \quad (3.1)$$

where \bar{v} is the normalized average dislocation velocity. The function F is intended to remain valid across the full range of parameter space (J^+, J^-, v_k, L, w) , *i. e.*, without restrictions to the underlying constitutive laws or parameter conditions, such as, for instance, low kink-pair nucleation rates.

The two limiting scenarios arising from drastic disparities between the kink velocity and the kink-pair nucleation rate can be readily formulated:

1. If the lateral migration of kinks significantly outpaces the kink-pair nucleation events, then any negative kink pairs will quickly collapse and the dislocation segment will advance by h for every nucleated positive kink pair:

$$\frac{\bar{v}}{h} = J^+ \quad (3.2)$$

2. On the contrary, if the migration of kinks is so slow that the dislocation moves by kink-pair nucleation only, then the negative kink pairs remain present long enough to compete with positive kink pairs. Therefore, an advancement of the dislocation line by h requires an excess of $\frac{L}{w}$ positive kink pairs to nucleate:

$$\frac{\bar{v}}{h} = \frac{1}{\frac{L}{w}(J^+ - J^-)^{-1}} = \frac{w}{L}(J^+ - J^-) \quad (3.3)$$

¹We make the simplifying assumption that positive and negative kink pairs share the same critical width.

Apart from these two limiting scenarios, the complex interplay between the stochastic kink-pair nucleation process and the lateral kink migration has so far precluded an analytical derivation of a general function F for the entire parameter space in Eq. (3.1).

This study presents a full-range formulation for the average dislocation velocity under the kink-pair mechanism, derived through probabilistic cellular automaton (CA) simulations. The propagation of conceptual dislocation segments are tracked across a wide range of conditions, and their average velocities are systematically fit using a hyperbolic tangent function. The resulting numerical approximation of the function F in Eq. (3.1) is valid for arbitrary combinations of (J^+, J^-, v_k, L, w) , without presumptions such as rare nucleation events. External dependencies such as stress or temperature can be introduced via the constitutive relations assigned to the five variables. By accommodating a wide range of kinetic laws, this general solution extends the applicability of dislocation mobility models and provides new insights into kink-governed deformation processes.

The methods of this study are presented in Section 3.2, followed by the simulation results and fitting process in Section 3.3. The underlying mechanism is discussed in Section 3.4.1. An example that demonstrates how to apply the proposed solution is provided in Section 3.4.2, and comparisons to existing approaches are given in Section 3.4.3. Lastly, Section 3.5 draws important conclusions.

3.2 Methods

Two exemplary snapshots (system configurations)² of the simulated glide process under contrasting kink-pair nucleation *vs.* kink lateral migration speed are given in Fig. 3.1. The slip plane is simplified as a rectangular cellular lattice of width L and infinite height, with each cell representing an area of wh . The dislocation separates the slipped area at the bottom from the unslipped area at the top. Cells in the unslipped area are rendered transparent, whereas any cell in the slipped area is shaded to reflect the amount of time since it became part of the slipped area, with the most recent slipped cells in black.

²Animations can be found in the GitHub repository given in Section 3.6.

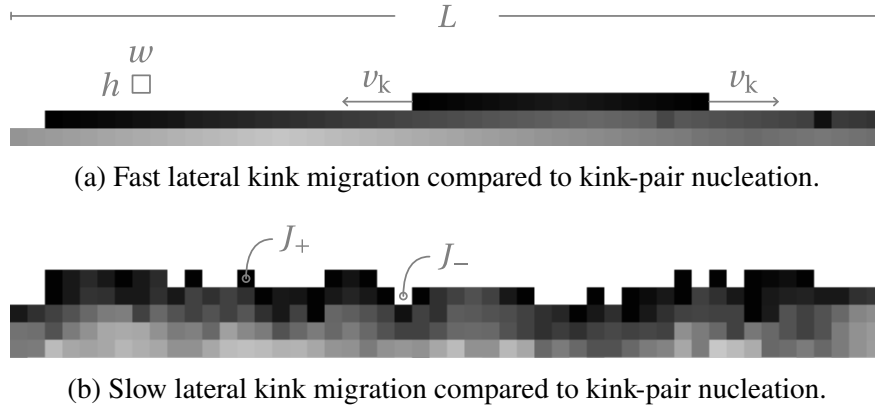


Figure 3.1 Snapshots of simulated dislocation profile (boundary between the white unslipped area at the top and the shaded slipped area at the bottom) for relatively fast (a) and slow (b) kink migration velocity v_k , respectively, under fixed positive and negative kink-pair nucleation rates (J^+ and J^-). The initial slipped area (the lightest gray area at the bottom) expands upward due to the nucleation of positive kink pairs and lateral kink migration. The most recently slipped area is rendered darkest and gets progressively lighter with every elapsed time step to illustrate the area expansion history. The cell dimension is critical kink pair width w by kink height h (not to scale). Both ends of the (fixed) dislocation segment of length L are considered to be perfect sinks for arriving kinks.

Along the dislocation segment, positive (upward) and negative (downward) kink pairs are formed at a mean rate J^+ and J^- , respectively, with the condition that $J^+ > J^-$, *i.e.*, the applied stress determines what is considered “positive.” Every kink moves laterally at a constant velocity v_k until meeting an opposite kink or the boundary of the simulation window, thereby always expanding the slipped area, *i.e.*, translating the dislocation line upwards.

Fig. 3.1a shows the scenario when the lateral kink migration significantly outpaces the kink pair nucleation, which results in an essentially straight dislocation line. The horizontal strips in the slipped area exhibit a constant gradient reflecting the constant v_k . Occasional abruptly darker cells are the remnants of collapsed negative kink pairs (*e.g.* in the second slipped row from the top). Fig. 3.1b, on the other hand, shows a rugged dislocation profile and a more random advance pattern (irregular shades) as the kink migration in the illustrated case is much less frequent than the nucleation of both positive and negative kinks.

Since kink pair nucleation events are considered to be uncorrelated, the number of such events during interval Δt , denoted as the random variable N , follows the Poisson distribution, *i.e.*, its

probability mass function is given by:

$$P(N_{\pm} = n_{\pm}) = \frac{(J^{\pm}\Delta t)^{n_{\pm}}}{n_{\pm}!} \exp(-J^{\pm}\Delta t) \quad (3.4)$$

for nucleation events of positive and negative kink pairs, respectively.

During each time step Δt :

1. Every kink moves laterally by $v_k\Delta t$ if there is still unslipped area next to it;
2. Two random samples r_{\pm} are individually drawn from the uniform distribution over $[0, 1)$, and the solution n_{\pm} of $P(N_{\pm} \leq n_{\pm}) = r_{\pm}$, respectively, becomes the number of new positive and negative kink pairs to be generated in Δt ;
3. The n_+ new positive kink pairs and n_- new negative kink pairs are generated in randomly shuffled sequence and positioned one by one at random locations along the dislocation segment, *i. e.*, along the boundary of the slipped area.

Since the propagation velocity of a dislocation segment can fluctuate widely on short time scales, the simulations of slipped area expansion are performed over a long enough period. The average dislocation propagation velocity up to the total simulation time t is then calculated as

$$\bar{v} = \frac{\text{slipped area}}{Lt} \quad (3.5)$$

Both Δt and t are selected such that neither a smaller Δt nor a larger t change the results by more than 1 %. To ensure statistical robustness, ten independent simulations were done for each explored point in the variable space (J^{\pm}, v_k, L, w, h) .

In this study, the values of all six variables are kept constant during individual simulations, *i. e.* are considered independent of the dislocation profile evolution.

3.3 Results

The critical kink-pair width w acts as a natural scaling factor for kink velocity v_k and segment length L , similarly to how kink height h does for the average velocity \bar{v} . Since the normalized

average velocity \bar{v} does not change with an arbitrary scaling of lengths by a in (J^+, J^-, av_k, aL, aw) , Eq. (3.1) can be reduced to a length-free form by choosing $a = w^{-1}$ such that

$$\bar{v} = f(J^+, \rho, v_k, \lambda) \quad (3.6)$$

with the normalized kink velocity $v_k = \frac{v_k}{w}$, normalized segment length $\lambda = \frac{L}{w}$, and net nucleation fraction $\rho = \frac{J^+ - J^-}{J^+}$. Consequently, the two theoretical limits resulting from relatively high and low kink migration velocity (Eqs. (3.2) and (3.3)) are then reduced to

$$\bar{v} = J^+, \quad \text{high-}v_k \text{ limit} \quad (3.7a)$$

$$\bar{v} = \frac{\rho}{\lambda} J^+, \quad \text{low-}v_k \text{ limit} \quad (3.7b)$$

In both cases, the normalized average velocity \bar{v} is proportional to the nucleation rate of positive kink pairs J^+ . Therefore, simulation results of \bar{v} are first plotted against J^+ for a given set of (ρ, v_k, λ) .

Fig. 3.2a presents exemplary results³ for four choices of (ρ, v_k, λ) as dots in different colors. All curves smoothly transition from the universal limiting behavior of relatively high kink velocity (blue line, Eq. (3.7a)) to different limiting behaviors at relatively low kink velocity that depend on the ρ/λ ratio (red lines, Eq. (3.7b)). The curves closely follow the high- v_k limit as long as

$$J^+ \leq \frac{v_k}{\lambda} = \frac{v_k}{L}, \quad (3.8)$$

which corresponds to the condition that a kink laterally sweeps the whole dislocation length before another positive kink pair nucleates. Consequently, the transition towards the intermediate regime begins near $J^+ = v_k/\lambda$ for all curves.

This is further demonstrated by Fig. 3.2b, where both axes are now rescaled by v_k/λ and all curves collapse onto the same high- v_k behavior. Moreover, curves that share a low- v_k limit (purple and black, orange and green) also collapse,⁴ suggesting that not only the low- v_k limits but also the *shape* of the transition zone is determined by the ρ/λ ratio.

³The ten replications under each condition deviate less than 1 % from each other and are visually indistinguishable at the scale of the figure, appearing as a single dot.

⁴The representation of purple and orange data is changed to solid lines in Fig. 3.2b to prevent them from being fully obscured by the black and green dots.

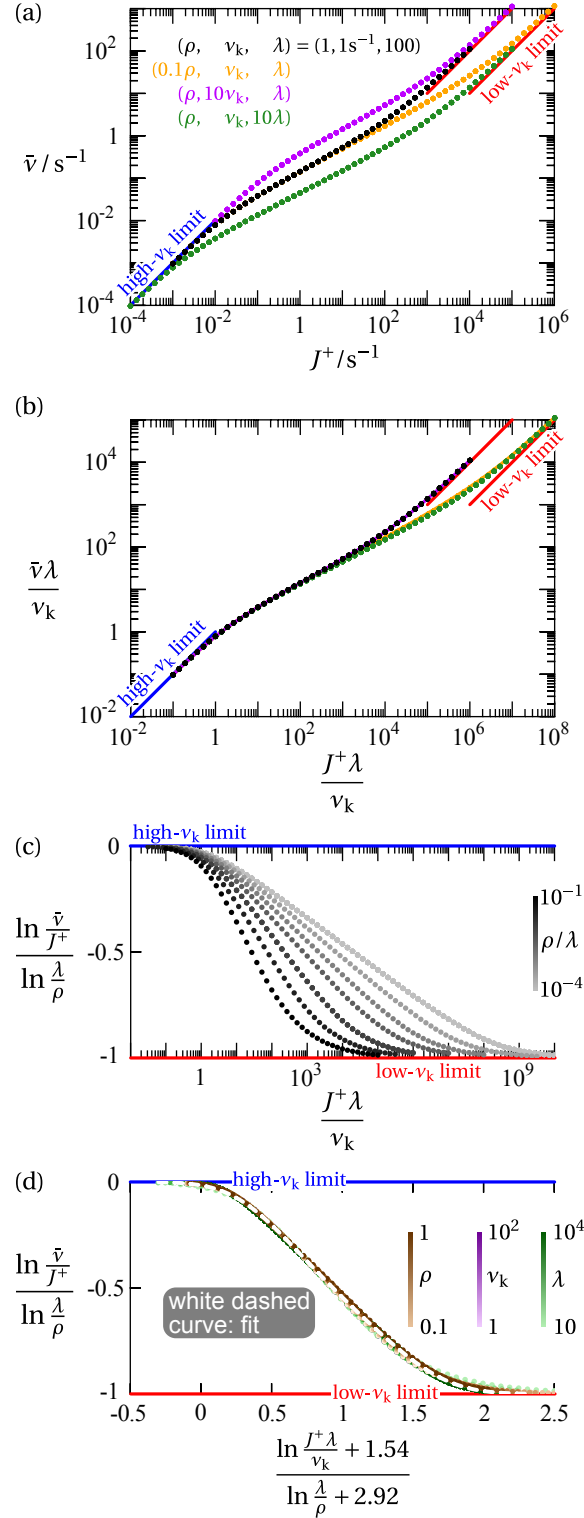


Figure 3.2 (a) Four exemplar $\bar{v} - J^+$ curves for (ρ, ν_k, λ) (black), $(0.1\rho, \nu_k, \lambda)$ (orange), $(\rho, 10\nu_k, \lambda)$ (purple), and $(\rho, \nu_k, 10\lambda)$ (green). (b) Normalizing both axes by ν_k/λ collapse the high- ν_k behavior. (c) Rescaling the ordinate to transform limits to align low- ν_k limits. (d) Transformation of the abscissa collapses all data points into a narrow band, enabling a fit (white curve) by a polynomially rescaled hyperbolic function given in Eq. (3.10).

Fig. 3.2c shows the operations to align the different low- ν_k limits. First, the ordinate is divided by the abscissa, resulting in a “shear” that transforms each limit to a constant value, and the limits become horizontal lines. Second, this rescaled ordinate is further normalized by the ratio between both limits (ρ/λ , see Eq. (3.7)), and all red lines are aligned. The gray-shaded curves illustrate the variation in the width of the transition zone for a range of logarithmically equispaced ρ/λ values. The transition width appears to be linearly related to the ρ/λ ratios on a log-log scale, suggesting the possibility to consolidate all curves through linearly rescaling the logarithm of the abscissa by $\ln(\rho/\lambda)$.

A successful fitting attempt⁵ is demonstrated in Fig. 3.2d with an abscissa transformation:

$$X = \frac{\ln \frac{J^+ \rho}{\nu_k} + 1.54}{\ln \frac{\lambda}{\rho} + 2.92} \quad (3.9)$$

The (asymmetrical sigmoid) master curve is then fitted by a polynomially rescaled hyperbolic tangent function⁶,

$$\frac{\ln \frac{\bar{v}}{J^+}}{\ln \frac{\lambda}{\rho}} = 0.5 (\tanh_{\text{poly}}(X) - 1), \quad (3.10)$$

where a satisfactory fitting is given as the white curve in Fig. 3.2d, using

$$\tanh_{\text{poly}}(X) = \tanh(2.06 - 3.74X + 2.37X^2 - 0.78X^3) \quad (3.11)$$

Combining Eqs. (3.9) to (3.11) gives the general solution of the average velocity of dislocations (Eq. (3.1)) as a function of the four constitutive variables of positive kink nucleation rate J^+ , net nucleation fraction ρ , kink migration rate ν_k , and normalized segment length λ :

$$\bar{v} = J^+ \sqrt{\lambda/\rho} \exp(\tanh_{\text{poly}}(X) - 1) \quad (3.12)$$

3.4 Discussion

3.4.1 Interpretation of the predicted behavior

As shown in Fig. 3.2a, the simulation results exhibit a transition between two limiting regimes (blue and red) during which the dislocation velocity is less than directly proportional to the kink-

⁵The optimization is done by minimizing the sum of the standard deviation of the curves’ ordinate values, and the standard deviations are calculated at 200 evenly spaced x -values sampled across the data range.

⁶There are other ways of rescaling the abscissa to address the asymmetrical feature of the sigmoid curve. Here we choose the straightforward polynomial expansion.

pair nucleation rate, *i.e.*, the slope across an intermediate regime is lower compared to the two limiting end cases. Starting at the high-kink-velocity limit (blue end on the left), the lateral kink migration is very fast compared to the kink pair nucleation rate such that lateral migration of a nucleated kink pair always finishes before the next kink-pair nucleation event. Clearly, this speed disparity cannot hold up towards higher and higher nucleation rates. Consequently, the relative increase in dislocation velocity with increasing nucleation rate progressively slows down compared to the high-kink-velocity limit because each positive kink-pair nucleation then only achieves partial lateral expansion, which results in a decreased slope. In this intermediate regime, the dislocation velocity is determined by an interplay of kink-pair nucleation *and* lateral migration. With a further increase in nucleation rate (or relative decrease in kink migration velocity) this regime transitions into the low-kink-velocity limit (red end on the right) where the kink migration velocity becomes so slow compared to the fast kink-pair nucleation that any dislocation advancement is solely caused by kink-pair nucleation. Hence, the dislocation velocity turns proportional to the kink-pair nucleation rate again, which results in the observed upward sloping.

The gradual changes in the sensitivity of the dislocation velocity over the large range of kink-pair nucleation rate observed in Fig. 3.2a, can be expected to result in corresponding variations of the nominal activation energy of dislocation velocity.

3.4.2 An example of model applicability

Relation (3.12) captures the full range of behavior without assuming limiting scenarios or any underlying kinetics other than the kink-pair mechanism, and is thus designed to accommodate a wide range of kinetic laws for the five variables in Eq. (3.1).

To demonstrate the model applicability, the same kinetic laws and associated parameters for a $\frac{1}{2}\langle 111 \rangle$ screw dislocation in Fe as those adopted by Boleininger et al. [13] is incorporated into Eq. (3.12), and the predicted dislocation velocity is compared with their analytical solution and kinetic Monte Carlo (kMC) simulations. In [13], the critical kink-pair width w is chosen as the Burgers vector length b . A single dislocation line of length L is partitioned into λ sites of length b , *i.e.* $L = \lambda b$, and each site can accommodate at most one kink. Each site can move forward (+) or

backward (-) by the kink height h via two processes:

1. nucleation of a kink pair at this site (and necessarily its neighbor) with rate

$$k_n^\pm = k_0 \exp\left[-\frac{2f_k(\pm\sigma, T)}{kT}\right], \quad (3.13)$$

2. motion of a kink across this site with rate

$$k_m^\pm = k_0(1 \pm \sigma/250 \text{ MPa}), \quad (3.14)$$

with the attempt frequency $k_0 = 10 \text{ ps}^{-1}$ and the free energy f_k of a kink [80] is given by

$$f_k = 0.33 \text{ eV} \left(1 - \frac{T}{700 \text{ K}} - \frac{\sigma/900 \text{ MPa}}{1 - T/700 \text{ K}}\right). \quad (3.15)$$

The above-listed two rates proposed in [13] are translated into $J^\pm = \lambda k_n^\pm$ and $v_k = h(k_m^+ - k_m^-)$,⁷ which then serve as input for Eq. (3.12).

Boleininger et al. [13] presume a low kink-pair nucleation rate and use a statistical mechanics approach to derive an approximate analytical expression for the mean dislocation velocity

$$\bar{v} = 2h\sqrt{\tilde{z}}(k_m^+ - k_m^-) \frac{I_1[2\lambda\sqrt{\tilde{z}}]}{I_0[2\lambda\sqrt{\tilde{z}}]}, \quad (3.16)$$

where $\tilde{z} = (k_n^+ + k_n^-) / 2k_0$ is the normalized average kink-pair nucleation rate, and I_n is the modified Bessel function of the first kind of order n . Parameters in Eqs. (3.13) to (3.15) are fitted to the kMC simulations.

Figure 3.3 compares kMC simulations (dots) and the statistical mechanics solution (Eq. (3.16), dashed lines) of [13] with the probabilistic CA solution (Eq. (3.12), solid line) proposed in the present study. The predicted temperature dependencies of dislocation velocity from both studies are very close to each other over a wide range of temperatures. However, towards high temperatures, the slopes of the probabilistic CA (solid) and statistical mechanics (dashed) curves start to differ, where the probabilistic CA solution predicts a faster increase of dislocation velocity with temperature.

⁷The unit step that scales the lateral kink velocity should *not* be h but b , as confirmed by Dr. Boleininger, but we follow the original expression of Boleininger et al. [13] in order to directly compare with their kMC simulations. This only slightly varies the results as h and b are within 40% of each other.

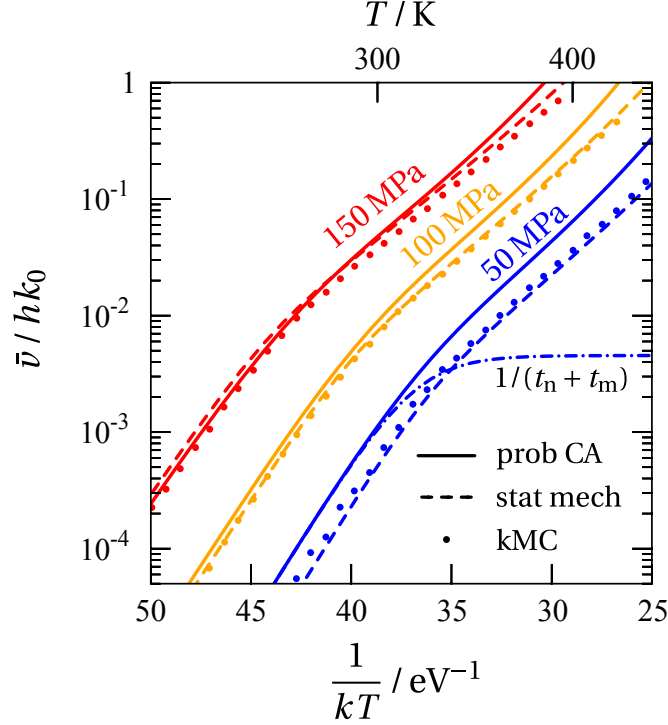


Figure 3.3 The average dislocation velocity resulting from the kMC simulations (dots) and corresponding statistical mechanics solution (dashed, Eq. (3.16)) of Boleininger et al. [13] in comparison to the probabilistic CA solution (solid, Eq. (3.12)) under three applied shear stresses and dislocation lengths of $250b$. An example of how Eq. (3.19) [18, 74] behaves is illustrated by the dash-dotted line, where t_n and t_m are the expected time for kink-pair nucleation and lateral sweeping by kink migration, respectively.

This difference is likely due to the presumption of rare kink-pair nucleation made by Boleininger et al. [13] in their solution, which becomes increasingly problematic at higher temperatures. Furthermore, the derivation of Eq. (3.16) is based on a simplification that precludes kink-pair nucleation within w of existing kinks. This might explain the divergence of dislocation velocity at high temperatures, which corresponds to a regime with relatively higher nucleation rates and more rugged dislocation profiles.

Overall, the agreement between both studies demonstrates that the probabilistic CA solution (Eq. (3.12)) yields consistent dislocation velocities when based on known input variables.

3.4.3 Comparison with alternative approaches

The classical approach to modeling screw dislocation velocity assumes a single thermally activated process characterized by a constant activation energy ΔG , leading to the expression

$$\bar{v} \propto \exp\left(-\frac{\Delta G}{kT}\right). \quad (3.17)$$

However, as shown in Fig. 3.3, every $\bar{v}-T^{-1}$ curve exhibits a distinct bend spanning approximately 50 K to 100 K, where the effective activation energy—evident from the slope—transitions smoothly from a higher constant value to lower ones with increasing temperature (left to right). This behavior indicates that assuming a constant ΔG becomes inadequate outside the low-temperature regime.⁸ We note that the bend in each curve in Fig. 3.3 happens around the point of the transition from the high-kink-velocity limit to the intermediate regime in Fig. 3.2a, which occurs at (*cf.* Eq. (3.8))

$$J^+ = \frac{v_k}{L}. \quad (3.18)$$

Therefore, Eq. (3.18) provides a criterion for the validity of using a constant ΔG : as soon as the stress or temperature causes a crossing of the transition point, it is advisable to use a more comprehensive model, such as Eq. (3.12), to properly account for the developing interplay between kink-pair nucleation and kink migration in the intermediate regime.

Another frequently employed mobility law [18, 74] for BCC screw dislocations is

$$\frac{\bar{v}}{h} = \frac{1}{t_n + t_m} = \frac{1}{\frac{1}{J^+} + \frac{L-w}{2v_k}}, \quad (3.19)$$

where t_n and t_m are the expected time for kink-pair nucleation and lateral sweeping by kink migration, respectively. Such an intuitive expression blends the rates of both processes and seems to account for the interplay between them. However, Eq. (3.19) implicitly assumes that only one kink pair exists at a time. Whereas this assumption is valid in the low-temperature limit—and yields identical results as Eq. (3.12)—it ignores the emergence of multiple kink pairs beyond that regime and, therefore, saturates at $2v_k/(L-w)$ (see the dash-dotted line in Fig. 3.3), which results in a constant velocity if the kink migration depends only on stress (such as in Eq. (3.14)).

⁸While approximating ΔG as locally constant over narrow temperature intervals may offer limited practical utility, such an approach is phenomenological and lacks a clear physical justification.

A method extending beyond the high-kink-velocity limit was proposed by Hirth and Lothe [31], based on kink diffusion theory. This model leads to

$$\bar{v} = v_0 \exp\left(-\frac{2f_k}{kT}\right), \quad \text{if } X \gg L, \quad (3.20a)$$

$$\bar{v} = v_0 \exp\left(-\frac{f_k}{kT}\right), \quad \text{if } X \ll L, \quad (3.20b)$$

where f_k is the free energy of a single kink, and X is the mean distance swept out by a nucleated kink pair before annihilation. These two asymptotic regimes are blended through harmonic averaging based on the dislocation segment length L . The condition $X \gg L$ in Eq. (3.20a) is identical to the high-kink-velocity limit where one nucleated kink pair completely sweeps the whole segment before the next nucleation event. In contrast, Eq. (3.20b) describes a regime in which multiple kink pairs are consistently present, leading to frequent kink collisions and mutual annihilation after short travel distances, analogous to the intermediate regime in Fig. 3.2a. Their proposed reduction of the activation energy from $2f_k$ to f_k is consistent with the observed change in slope between the high-kink-velocity limit and the intermediate regime in Fig. 3.2a. However, it is worth stressing that the nominal activation energy in the intermediate regime is *not* a predetermined quantity, such as f_k , but results inevitably/organically from the transition between two parallel asymptotes, *i.e.*, the transition from blue to red limit.

Lastly, the statistical mechanics model offered by Boleininger et al. [13] (Eq. (3.16)) covers the high-kink-velocity regime well and extends to the intermediate regime, as shown in Fig. 3.3. Nevertheless, in addition to the divergence observed at the high temperature end, a practical concern is the numerical overflow of the Bessel functions encountered⁹ at higher temperatures. Furthermore, this statistical mechanics model does not inherently recover the high-kink-velocity limit (Eq. (3.2), blue end), because the normalized kink velocity ($k_m^+ - k_m^-$) directly scales the overall dislocation velocity (*cf.* Eq. (3.16)) rather than being an asymptotic contribution. As a result, the predicted dislocation velocity remains sensitive to the chosen kink migration law even in regimes where it should not, thereby limiting the robustness of the model under varying kinetic inputs.

⁹For the exemplar conditions in Section 3.4.2, both I_0 and I_1 overflow in Python soon after the curves reach the top end of the figure frame.

3.5 Conclusions

This study addressed the lack of a general mobility law that accurately captures dislocation motion via the kink-pair mechanism across the full spectrum of nucleation-to-migration rate ratios. By formulating the average dislocation velocity as a function of kink-pair nucleation rates, kink migration velocity, dislocation segment length, kink-pair width, and kink height, the model provides a full-range solution based on systematic fitting of results from probabilistic cellular automaton simulations. The proposed solution does not rely on limiting assumptions or averaging of asymptotic regimes, and therefore enables a more accurate prediction of the dislocation velocity and supports robust modeling of temperature- and time-dependent plastic responses. Its compatibility with a wide range of kinetic laws for the above-listed five variables extends the applicability to BCC metals at elevated temperatures and to other material systems governed by the kink-pair mechanism. Future work may incorporate refinements, such as trapezoidal kink-pair shapes or alternative definitions of available nucleation sites, to further enhance physical fidelity and flexibility.

3.6 Data Availability

All scripts employed to generate the data that support the findings of this study are available at https://github.com/CathyBing/KP_velocity.

CHAPTER 4

A COMPREHENSIVE CONSTITUTIVE MODEL FOR BCC METALS

4.1 Introduction

The behavior of dislocations plays a central role in the plastic deformation of crystalline materials. Studies have shown that the crystallographic distribution of dislocations among slip systems strongly influences the plastic response, suggesting that effective crystal plasticity models should be capable of tracking both the mobility and evolution of dislocation populations throughout deformation [56, 90]. The need for a comprehensive constitutive model that can accurately predict the dislocation dynamics under complex thermomechanical conditions becomes especially important in the context of cavity formation and other manufacturing processing scenarios.

In BCC metals, the underlying dislocation mechanisms are notably complex. A key aspect is the fundamental difference in behavior between edge and screw dislocations. As discussed in Section 1.4, edge dislocations generally have much lower Peierls stresses compared to screw dislocations, which leads to higher mobility. For instance, phase-field dislocation dynamics simulations of niobium by Jones et al. [33] demonstrate that under applied stress, edge dislocations respond almost instantaneously, while screw dislocations exhibit a delay due to their kink-pair-controlled motion. As a result, edge dislocations can quickly leave the crystal, often accumulating at free surfaces, whereas screw dislocations remain and dominate the plastic strain rate [29, 77]. This mobility disparity has been confirmed through both *in situ* electron microscopy and atomistic simulations [41, 77, 42, 95].

Because of this well-known distinction in mobility, most conventional crystal plasticity models do not differentiate between edge and screw dislocation populations in the context of BCC metals. Mobility laws are frequently based solely on screw dislocation behavior, modeled through the kink-pair mechanism, while edge dislocations are often neglected [36, 18]. This simplification limits the ability of such models to capture critical features of plastic flow, particularly under more complex or extreme conditions. For example, Chen et al. [21] showed that in high-entropy BCC alloys, both edge and screw dislocations contribute comparably to strengthening due to nanoscale

trapping effects. Similarly, Jones et al. [33] reported that at higher homologous temperatures, the mobilities of edge and screw dislocations tend to converge. In addition, it is commonly claimed that above the critical temperature where edge and screw mobilities become nearly equal, the BCC material behaves “FCC-like”.

At the atomistic level, density functional theory and molecular dynamics simulations have revealed that screw dislocations in BCC metals possess non-planar core structures, spreading symmetrically across several slip planes intersecting along the $\langle 111 \rangle$ direction [88, 24, 87, 93]. This unique core configuration promotes frequent cross-slip events, which in turn introduce additional complexity in tracking dislocation mobility and evolution across slip systems.

To address these challenges, a comprehensive dislocation-density-based crystal plasticity model for BCC metals is developed. This model explicitly distinguishes between edge and screw dislocation populations and incorporates the kink-pair mobility framework developed in Chapter 3. It features separate mobility laws and density evolution equations for each dislocation character, enabling more accurate representations of thermally activated screw motion and relatively athermal edge glide. Additional mechanisms, such as screw cross-slip and edge climb, are also incorporated into the density evolution laws. Cross-slip is implemented in a statistical manner, through redistribution of screw dislocation density across slip systems without additional energy barrier, reflecting its inherently stochastic nature. Moreover, the model includes character-specific parameters such as distinct annihilation distances for edge and screw dipoles, being consistent with observations that edge dipoles annihilate over shorter distances than screw dipoles [95].

In summary, this physically informed model is designed to capture the complex plastic behavior of BCC metals across a wide range of thermomechanical conditions. All features are implemented as modular and switchable, providing a flexible platform for systematically assessing the role of various mechanisms in different material systems.

4.2 Constitutive model

The kinematic framework as the foundation of the following model is introduced in Section 1.2.2.

Assuming all plastic deformation in the current scheme is due to slip, the plastic velocity gradient

\mathbf{L}_p is given by the additive combination of shear contributions from all $N_{\text{slip}} = 12 \langle 111 \rangle \{110\}$ slip systems¹ (indexed by α and implicitly summed over repeated indices)

$$\mathbf{L}_p = \dot{\gamma}^\alpha \mathbf{m}^\alpha \otimes \mathbf{n}^\alpha = (\dot{\gamma}_e^\alpha + \dot{\gamma}_s^\alpha) \mathbf{m}^\alpha \otimes \mathbf{n}^\alpha \quad (4.1)$$

where $\dot{\gamma}$ is the shear rate, \mathbf{m} and \mathbf{n} are unit vectors along the slip direction and the slip plane normal, respectively, and the contribution from edge ($\dot{\gamma}_e$) and screw ($\dot{\gamma}_s$) characters are explicitly disaggregated.

To account for the non-Schmid effect that is a prominent feature in BCC metals, the resolved shear stress (RSS) τ is modified following the work by Koester et al. [35]:

$$\tau_e^\alpha = \mathbf{S} : \mathbf{m}^\alpha \otimes \mathbf{n}^\alpha \quad (4.2a)$$

$$\begin{aligned} \tau_s^\alpha = & \mathbf{S} : \mathbf{m}^\alpha \otimes \mathbf{n}^\alpha + a_1 \mathbf{S} : \mathbf{m}^\alpha \otimes \mathbf{n}_1^\alpha + a_2 \mathbf{S} : (\mathbf{n}^\alpha \times \mathbf{m}^\alpha) \otimes \mathbf{n}^\alpha + \\ & a_3 \mathbf{S} : (\mathbf{n}_1^\alpha \times \mathbf{m}^\alpha) \otimes \mathbf{n}_1^\alpha + a_4 \mathbf{S} : \mathbf{n}^\alpha \otimes \mathbf{n}^\alpha + \\ & a_5 \mathbf{S} : (\mathbf{n}^\alpha \times \mathbf{m}^\alpha) \otimes (\mathbf{n}^\alpha \times \mathbf{m}^\alpha) + a_6 \mathbf{S} : \mathbf{m}^\alpha \otimes \mathbf{m}^\alpha \end{aligned} \quad (4.2b)$$

where \mathbf{S} is the second Piola–Kirchhoff stress, a_1, \dots, a_6 are parameters determining the non-Schmid modification (given in Table 4.4), and \mathbf{n}_1 is a pre-selected $\{110\}$ plane normal which is related to \mathbf{n} by a 60° rotation about \mathbf{m} . The resolved shear stress for edge dislocations τ_e is still the classical Schmid projection (Eq. (4.2a)), as no non-Schmid effect has been reported for the edge character, whereas due to the non-planar core structure, the screw dislocations typically experience unsymmetrical resistance to positive and negative shear directions, addressed by the modulated resolved shear stress (Eq. (4.2b)).

The passing stress τ_{pass} or the slip resistance due to latent and self-hardening is calculated using the dislocation-density-based hardening law [64]

$$\tau_{\text{pass}}^\alpha = \mu b \left(\sum_{\alpha'=1}^{N_{\text{slip}}} \xi_{\alpha\alpha'} \rho^{\alpha'} \right)^{\frac{1}{2}} \quad (4.3)$$

¹The current model only considers slip along $\{110\}$ planes, following the argument made by ?] for tungsten that an elementary glide on a $\{112\}$ plane is a composite of two elementary steps on alternate $\{110\}$ planes. This may not be monoversally true for BCC metals, but we are using it here for simplicity and $\{112\}$ could be added without too much work.

	D1	C1	B2	A2	A3	C3	B4	D4	A6	D6	B5	C5
D1	1	3	6	6	7	5	4	2	4	2	7	5
C1	3	1	6	6	4	2	7	5	7	5	4	2
B2	6	6	1	3	5	7	2	4	5	7	2	4
A2	6	6	3	1	2	4	5	7	2	4	5	7
A3	7	5	4	2	1	3	6	6	2	4	7	5
C3	4	2	7	5	3	1	6	6	5	7	4	2
B4	5	7	2	4	6	6	1	3	7	5	2	4
D4	2	4	5	7	6	6	3	1	4	2	5	7
A6	5	7	4	2	2	4	7	5	1	3	6	6
D6	2	4	7	5	5	7	4	2	3	1	6	6
B5	7	5	2	4	7	5	2	4	6	6	1	3
C5	4	2	5	7	4	2	5	7	6	6	3	1

Table 4.1 Dislocation interaction matrix $\xi_{\alpha\alpha'}$ for BCC metals [44]. Schmid and Boas notation is used to identify slip systems.

where μ is the shear modulus, b is the length of the Burgers vector, and the coefficient matrix $\xi_{\alpha\alpha'}$ [44] characterizes the interaction between slip systems (see Table 4.1).

The effective resolved shear stress τ_{eff} is the exceeding part of τ compared to τ_{pass} ,

$$\tau_{\text{eff}}^{\alpha} = \begin{cases} |\tau^{\alpha}| - \tau_{\text{pass}}^{\alpha} & \text{for } |\tau^{\alpha}| > \tau_{\text{pass}}^{\alpha} \\ 0 & \text{for } |\tau^{\alpha}| \leq \tau_{\text{pass}}^{\alpha} \end{cases}, \quad (4.4)$$

Within a certain distance (\hat{d}), two monopolar (mobile) dislocations of the same character and opposite signs can form a dipolar configuration, whose movement doesn't considerably contribute to the deformation anymore². In our framework, on top of the edge-screw disaggregation, the dislocation density is categorized into monopolar and dipolar status, depending on the pairing status:

$$\begin{aligned} \rho &= \rho_e + \rho_s \\ &= \rho_{m,e} + \rho_{m,s} + \rho_{d,e} + \rho_{d,s}. \end{aligned} \quad (4.5)$$

For screw dislocations, slip systems are grouped according to Burgers vector, see Table 4.2. Screw population within a cross-slip group is unified, for two considerations:

1. Due to the non-planar core structure, it is likely that a line segment of screw character features 3 slip systems at the same time;

²Except for the limited increase of slipped area when the dipole coalescence.

	cross-slip groups											
	A			B			C			D		
	A2	A3	A6	B2	B4	B5	C1	C3	C5	D1	D4	D6
slip system												
slip direction	[111]			[111]			[111]			[111]		
slip plane	(011)	(101)	(110)	(011)	(101)	(110)	(011)	(101)	(110)	(011)	(101)	(110)

Table 4.2 12 $\langle 111 \rangle \{110\}$ slip systems are grouped into four cross-slip groups.

2. There should not be any imposed energy barrier on cross-slip comparing to slip.

The second point is disputable, as it is well-accepted to describe the mechanism of cross-slip with an exponential probability function featuring an activation energy ΔG_{cs} , *i.e.*

$$P \propto \exp\left(\frac{\Delta G_{cs}}{kT}\right), \Delta G_{cs} = -V(\tau_{crit} - \tau), \quad (4.6)$$

where V is the activation volume, τ is the RSS on the cross-slip plane, and τ_{crit} is the critical stress for cross slip, sometimes chosen as the critical RSS at the onset of stage III on the stress-strain curve as proposed by Kubin et al. [37], or calculated otherwise with a presumed semi-circular configuration of cross-slip propagation [65]. The former choice technically eliminates the possibility of cross-slip before stage III, whereas cross-slip was observed as early as in stage I; and the latter one is only correct if the screw and edge characters have the same velocity, which is not true for BCC metals. Either way, the required energy is generally quite considerable, whereas cross-slip is not a rare event to be observed in BCC materials. Moreover, given the non-planar core structure, screw dislocations should view the three cross-slip slip systems rather impartially, *i.e.*, there should not be any conceptual distinction between slip and cross-slip.

The usage of the cross-slip probability function P has been amended to circumvent its implied high energy barrier [2, 57]. Instead of a solid indicator determining whether a cross-slip event would happen, it was used to calculate the *relative* probability on each cross-slip system, and a tendency of cross-slipping onto the high- P system is assumed, which is actually an indirect comparison of RSS on each cross-slip system. The redistribution of screw dislocations is consequently determined.

In our model, the screw dislocation is not distinguished within each cross-slip group. Plastic flow of monopolar screw dislocations will be partitioned according to the RSS weight. In other

words, it is assumed that the unified cross-slip monopolar screw population has the tendency to (cross-)slip onto the plane that has higher RSS, and the resulted plastic flow will distribute according to the relative RSS on each possible cross-slip slip system. During each strain step, in cross-slip group Ψ , the density of monopolar screw dislocation that slips on slip system α is

$$\rho_{m,s}^{\alpha} = \frac{\tau_{\text{eff}}^{\alpha}}{\sum_{\alpha' \in \Psi} \tau_{\text{eff}}^{\alpha'}} \rho_{m,s}^{\Psi} \quad (4.7)$$

In addition, interaction between screw dislocations is not limited to the same slip system but the same cross-slip group, *e.g.* monopoles forming dipoles, spontaneous annihilation, *etc.*

4.2.1 Mobility laws

Following the Orowan equation [53], the contributions of edge and screw monopoles towards the total shear rate $\dot{\gamma}$ are analyzed separately,

$$\dot{\gamma}^{\alpha} = \rho_{m,e}^{\alpha} b v_e^{\alpha} + \rho_{m,s}^{\alpha} b v_s^{\alpha}, \quad (4.8)$$

where v_e and v_s are the velocity of monopolar edge and screw dislocations, respectively, in contrast to the average velocity v when the edge and screw characters are not individually considered. Note that only the movement of monopolar dislocations causes plastic shear, as the synchronized movement of a pair dislocations in dipolar configuration cancels out each other.

Note that dislocation velocity predicted by molecular dynamics (MD) simulation is in general too fast to be realistic. This is mainly due to the limited timescale in MD simulation, where the deformation has to be explosive. As a result, the velocity of dislocation is ultra fast and should not be used as reference in continuum modeling of crystal plasticity.

4.2.1.1 Edge mobility law

The controlling factor of edge dislocation mobility is the lattice friction, while other mechanisms such as kink nucleation and climb are not significant enough to be included in this model. The glide mechanism has been reported to stay the same under a wide range of temperatures [33], and being mostly athermal [14, 42]. Following Lothe [40], in non-relativistic regime, a dislocation segment moving with uniform velocity v experiences the dissipative friction or drag force per unit length

f_{drag} according to the viscous damping law

$$f_{\text{drag}} = -B(T)v \quad (4.9)$$

where $B(T)$ is the drag coefficient as a function of temperature T and independent of v . As proposed by Swinburne et al. [81], the drag coefficient can be written in the form

$$B(T) = B_0 + B_1T \quad (4.10)$$

with a constant term B_0 that dominates for nanoscale defects, and a linear term $B_1 T$ to include the temperature dependence that is appreciable only for dislocations on an extended scale. As a result of force equilibrium, the velocity of monopolar edge dislocation v_e is given by

$$v_e = \frac{\tau_{\text{eff}}b}{B_0 + B_1T}, \quad (4.11)$$

where $\tau_{\text{eff}} b$ is the glide force per unit length of dislocation.

4.2.1.2 Screw mobility law

In BCC metals, screw dislocations are much less mobile than the edge character, and their motion is enabled by the nucleation of kink-pairs and their lateral expansion. With low Peierls' barrier to the kink motion in metals, the kink velocity v_k is given similar to Eq. (4.11) as

$$v_k = \frac{\tau_{\text{eff}}b}{B_k} \quad (4.12)$$

where B_k is the constant drag coefficient for kink, equivalent to the term B_0 in Eq. (4.10), as the temperature-dependent term could be safely ignored for short dislocation segments.

The positive kink-pair nucleation rates J^+ follow an Arrhenius formulation:

$$J^+ = \frac{\nu_{\text{kp}}(\lambda - w)}{b} \exp\left(-\frac{\Delta G_{\text{kp}}(\tau_{\text{eff}})}{kT}\right), \quad (4.13)$$

where ν_{kp} is the attempt frequency, λ is the average segment length of screw dislocations, w is the typical separation between a nucleated kink pair, ΔG_{kp} is the Gibbs free energy of kink pair formation at the given stress state, and k is the Boltzmann's constant. λ is represented by the mean free path of forest dislocations, which estimates the segment length between obstacles (nodes):

$$\lambda^\alpha = \left(\sum_{\alpha'=1}^{N_{\text{slip}}} \left(\left| \mathbf{n}^\alpha \cdot \mathbf{n}^{\alpha'} \times \mathbf{m}^{\alpha'} \right| \rho_e^{\alpha'} + \left| \mathbf{n}^\alpha \cdot \mathbf{m}^{\alpha'} \right| \rho_s^{\alpha'} \right) \right)^{-\frac{1}{2}} \quad (4.14)$$

Note that the projection along the plane normal for edge and screw forest dislocations is different. The stress dependence of $\dot{\gamma}$ is a consequence of the stress dependence of ΔG_{kp} , which can be formulated following Po et al. [60],

$$\Delta G_{\text{kp}} = \Delta H_{\text{kp}} - T\Delta S_{\text{kp}} = \Delta H_0 \left\{ \left[1 - \left(\frac{\tau_{\text{eff}}}{\tau_{\text{P}}} \right)^p \right]^q - \frac{T}{T_0} \right\} \quad (4.15)$$

where ΔH_{kp} is the formation enthalpy, ΔS_{kp} is the corresponding entropy. The power-law term is introduced by Kocks [34] with ΔH_0 being the activation enthalpy under zero stress, p and q define the shape of the dislocation obstacle, $0 < p \leq 1$ and $1 \leq q \leq 2$ for most cases, τ_{P} is the Peierls stress needed to overcome the obstacle without any thermal activation, T_0 is the athermal transition temperature above which the energy barrier for kink-pair nucleation is guaranteed to vanish independent of stress.

The average screw dislocation velocity v_s is then determined by Eq. (3.12).

4.2.2 Density evolution laws

Three aspects are considered in the evolution of monopolar dislocations:

1. the multiplication ($\dot{\rho}_{\text{multi}}$) due to the expansion of the slipped area,
2. the spontaneous annihilation ($\dot{\rho}_{\text{anni}}$) along with slipped area coalescence when two opposite monopoles are too close to each other (distance $< \check{d}$),
3. the formation of (temporarily/relatively) stable dipoles ($\dot{\rho}_{\text{form}}$) when the distance is within the range $[\check{d}, \hat{d}]$ determined by the current stress state.

The time derivative of monopole density ($\dot{\rho}_{\text{m}}$) for each slip system α can accordingly be written as

$$\dot{\rho}_{\text{m}}^{\alpha} = \dot{\rho}_{\text{multi}}^{\alpha} - \dot{\rho}_{\text{anni}}^{\alpha} - \dot{\rho}_{\text{form}}^{\alpha} \quad (4.16)$$

For dipolar evolution, the contribution from monopoles ($\dot{\rho}_{\text{form}}$) could be sacrificed by

1. the simultaneous annihilation when

Thus,

$$\dot{\rho}_d^\alpha = \begin{cases} \dot{\rho}_{\text{stable}}^\alpha - \dot{\rho}_{\text{m-d}}^\alpha - \dot{\rho}_{\text{cl}}^\alpha & \text{for edge dipoles} \\ \dot{\rho}_{\text{stable}}^\alpha - \dot{\rho}_{\text{m-d}}^\alpha - \dot{\rho}_{\text{cs}}^\alpha & \text{for screw dipoles} \end{cases}, \quad (4.17)$$

while a dislocation segment belonging to a dipole pair could still be approached by an opposite monopole and spontaneously annihilate, and the previously paired dipolar dislocation becomes monopolar, resulting in the unchanged monopole density and decreased dipole density ($\dot{\rho}_{\text{m-d}}^\alpha$), and a pair of dipolar dislocations can move out of the original glide plane to annihilate with each other, by climb ($\dot{\rho}_{\text{cl}}^\alpha$) for edge dipoles or cross-slip ($\dot{\rho}_{\text{cs}}^\alpha$) for screw dipoles, which is considered to be much slower than the above mentioned spontaneous reactions. The following treatment of these terms is mainly an extrapolation of the proposition of Eisenlohr [26], Blum and Eisenlohr [11], except for the cross-slip aspect $\dot{\rho}_{\text{cs}}$.

4.2.2.1 Multiplication $\dot{\rho}_{\text{multi}}$

$\dot{\rho}_{\text{multi}}^\alpha$ is characterized by introducing a ratio Λ^α ³ of slipped area dA^α per generated monopolar dislocation length $d\lambda^\alpha$

$$\frac{1}{\Lambda^\alpha} = \frac{d\lambda^\alpha}{dA^\alpha} = \frac{\dot{\rho}_{\text{multi}}^\alpha}{\dot{\gamma}^\alpha/b} \propto \frac{1}{\text{dislocation spacing}} := \frac{1}{D} + \frac{1}{\lambda^\alpha}, \quad (4.18)$$

where D is the effective grain size and λ is the spacing between forest dislocations, which is given by

$$\frac{1}{\lambda} = \frac{1}{i} \left(\sum_{\alpha'=1}^{N_{\text{slip}}} \left(\mathbf{n}^\alpha \cdot \mathbf{m}^{\alpha'} \rho_s^{\alpha'} + \mathbf{n}^\alpha \cdot \mathbf{n}^{\alpha'} \times \mathbf{m}^{\alpha'} \rho_e^{\alpha'} \right) \right)^{\frac{1}{2}} \quad (4.19)$$

where i is a fitting parameter that represents the number of dislocations passed by a dislocation before being trapped by a forest dislocation.

The multiplication rate $\dot{\rho}_{\text{multi}}$ is calculated by

$$\dot{\rho}_{\text{multi,e}}^\alpha = \frac{\dot{\gamma}_s^\alpha}{b\Lambda^\alpha} \quad (4.20a)$$

$$\dot{\rho}_{\text{multi,s}}^\alpha = \frac{\dot{\gamma}_e^\alpha}{b\Lambda^\alpha} \quad (4.20b)$$

as the slip of edge and screw dislocations multiplies the screw and edge characters, respectively.

³In this model, strain hardening is described using a dislocation Mean Free Path (Λ) approach.

4.2.2.2 Spontaneous reaction $\dot{\rho}_{\text{form}}$, $\dot{\rho}_{\text{stable}}$, and $\dot{\rho}_{\text{m-d}}$

A critical glide plane distance \hat{d} below which two opposite monopoles form a dipole is a function of effective resolved shear stress τ_{eff} :

$$\hat{d}_e^\alpha = \frac{\mu b}{8\pi(1-\nu)|\tau_{\text{eff}}^\alpha|} \quad (4.21a)$$

$$\hat{d}_s^\alpha = \frac{\mu b}{4\pi|\tau_{\text{eff}}^\alpha|} \quad (4.21b)$$

Another critical glide plane distance \check{d} below which a dipole would annihilate spontaneously is typically a multiple of the Burgers vector:

$$\check{d}_e^\alpha = D_{\text{anni,e}}^\alpha b \quad (4.22a)$$

$$\check{d}_s^\alpha = D_{\text{anni,s}}^\alpha b \quad (4.22b)$$

where D is a self-determined coefficient, which could be used to control the annihilation rate in the simulation.

4.2.2.3 Dipole climb velocity v_{cl}

The vacancy diffusion enabled dislocation climb velocity v_{cl} is calculated as

$$v_{\text{cl}}^\alpha = \mu D_0 \exp\left(-\frac{\Delta G_{\text{cl}}}{kT}\right) \frac{V_{\text{at}}}{\pi(1-\nu)kT} \frac{1}{\hat{d}_e^\alpha + \check{d}_e^\alpha} \quad (4.23)$$

where ΔG_{cl} is the activation energy for dislocation climb, here taken as a constant, D_0 is the pre-factor of the self-diffusion coefficient, and V_{at} is the atomic volume.

4.2.2.4 Dipole cross slip velocity v_{cs}

We propose that, instead of that elastic bow-out, the cross-slip should follow the same kink-pair mechanism as screw monopoles. Unlike climb being a vacancy-diffusion determined process which is a different mechanism from glide, cross-slip of screw dipoles are still glide in nature, so intrinsically we should not need a brand-new rule for cross-slip. The only difference is the modification of driving force, where the attraction between a pair of dipolar screw dislocation reinforces their approaching to each other by cross-slip, and the glide velocity on the cross-slip plane will increase due to the increased stress.

Parameter	Definition	Value	unit
C_{11}	elastic stiffness tensor element [82]	243.6	GPa
C_{12}	<i>ibid.</i>	130.2	GPa
C_{44}	<i>ibid.</i>	27.9	GPa
μ	shear modulus	37.5	GPa
a_0	lattice parameter of BCC niobium	3.3	Å
b	magnitude of Burgers vector for $\langle 111 \rangle \{110\}$ slip family	$\frac{\sqrt{3}}{2}$	a_0
T	temperature	300	K
T_m	melting temperature	2750	K
D	grain size	5×10^{-5}	m
i	Adj. parameter for distance between two forest dislocations	100	-
ν	Poisson ratio	$\frac{1}{3}$	-

Table 4.3 General parameters representing BCC Nb used in the model.

Therefore, v_{cs} is determined by the same process as described in Section 4.2.1.2 with modified stress state.

4.2.2.5 Summary of the constitutive laws

Apply above analysis to Eq. (4.16) and Eq. (4.17), we have:

$$\dot{\rho}_{m,e}^{\alpha} = \frac{|\dot{\gamma}_e^{\alpha}|}{b\Lambda^{\alpha}} - \frac{2\hat{d}_e^{\alpha}}{b}\rho_{m,e}^{\alpha}|\dot{\gamma}_e^{\alpha}| \quad (4.24a)$$

$$\dot{\rho}_{m,s}^{\alpha} = \frac{|\dot{\gamma}_s^{\alpha}|}{b\Lambda^{\alpha}} - \frac{2\hat{d}_s^{\alpha}}{b}\rho_{m,s}^{\alpha}|\dot{\gamma}_s^{\alpha}| \quad (4.24b)$$

$$\dot{\rho}_{d,e}^{\alpha} = \frac{2(\hat{d}_e^{\alpha} - \check{d}_e^{\alpha})}{b}\dot{\rho}_{m,e}^{\alpha}|\dot{\gamma}_e^{\alpha}| - \frac{2\check{d}_e^{\alpha}}{b}\rho_{d,e}^{\alpha}|\dot{\gamma}_e^{\alpha}| - \rho_{d,e}^{\alpha}\frac{2v_{cl}^{\alpha}}{\hat{d}_e^{\alpha} - \check{d}_e^{\alpha}} \quad (4.24c)$$

$$\dot{\rho}_{d,s}^{\alpha} = \frac{2(\hat{d}_s^{\alpha} - \check{d}_s^{\alpha})}{b}\dot{\rho}_{m,s}^{\alpha}|\dot{\gamma}_s^{\alpha}| - \frac{2\check{d}_s^{\alpha}}{b}\rho_{d,s}^{\alpha}|\dot{\gamma}_s^{\alpha}| - \rho_{d,s}^{\alpha}\frac{2v_{cs}^{\alpha}}{\hat{d}_s^{\alpha} - \check{d}_s^{\alpha}} \quad (4.24d)$$

4.2.3 Parameters

Since the model is currently under the calibration process, this subsection presents representative parameters for pure niobium as a demonstrative case. Table 4.3 summarizes the general material properties applied to both edge and screw dislocations, while Table 4.4 lists the character-specific parameters used to distinguish their respective behaviors.

4.3 Implementation

The proposed crystal plasticity model has been implemented as a modular extension within the DAMASK (Düsseldorf Advanced Material Simulation Kit, [68]) framework. The formulation

Parameter	Definition	Edge	Screw	unit
a_1	coefficient in Eq. (4.2a) for non-Schmid resolved stress	-	0.61	-
a_2	<i>ibid.</i>	-	0.23	-
a_3	<i>ibid.</i>	-	0.55	-
a_4	<i>ibid.</i>	-	0.11	-
a_5	<i>ibid.</i>	-	0.09	-
a_6	<i>ibid.</i>	-	-0.2	-
$\rho_{\text{mono},0}$	initial monopolar dislocation density	10^{11}	10^{11}	m^{-2}
$\rho_{\text{di},0}$	initial dipolar dislocation density	10^{11}	10^{11}	m^{-2}
B_0	temperature independent part of friction coefficient	4×10^{-4}	-	Pa s
B_1	temperature dependent part of friction coefficient	1×10^{-6}	-	Pa s K ⁻¹
B_k	(temperature independent) friction coefficient of kink	-	8×10^{-5}	Pa s
h	distance between two consecutive Peierls valleys	$\frac{\sqrt{6}}{3}$	-	a_0
w	width of the kink pair	-	11	b
ν_{kp}	attempt frequency of kink pair nucleation	-	9.1×10^{11}	s^{-1}
ΔH_0	activation enthalpy under zero stress	-	2.72×10^{-19}	J
τ_p	Peierls stress	-	20	MPa
p	p exponent defining the shape of the dislocation obstacle	-	0.86	-
q	q exponent in glide velocity	-	1.69	-
T_0	athermal transition temperature	-	0.8	T_m
D	coefficient of spontaneous annihilation distance	10	10	-
D_0	pre-factor for self-diffusion	1.1×10^{-4}	-	-
ΔG_{cl}	Activation energy for climb	4.5×10^{-19}	-	J
V_{at}	atomic volume	1	-	b^3

Table 4.4 Plasticity parameters that are separately determined for edge and screw characters.

allows for flexible integration with existing DAMASK capabilities and supports simulation of complex deformation processes in BCC metals.

Key physical mechanisms (*e.g.*, cross-slip and climb) are implemented as optional features. These mechanisms can be activated or deactivated via user-defined input settings, enabling controlled investigations into their individual and collective effects on plastic behavior.

4.4 Summary

A comprehensive dislocation-density-based crystal plasticity model tailored for BCC metals is presented. Motivated by the complex and character-dependent dislocation behavior in BCC systems, the model explicitly distinguishes between edge and screw dislocation populations and incorporates separate mobility laws and density evolution equations for each dislocation character.

Additional mechanisms, such as cross-slip for screws and climb for edges, are embedded into the evolution framework, enhancing the model's physical fidelity. Character-specific parameters,

such as annihilation distances, are also implemented to reflect the distinct annihilation behaviors observed in atomistic simulations.

The model architecture is modular, allowing individual physical mechanisms to be activated or deactivated. This flexibility enables systematic exploration of their influence on plastic behavior under various thermomechanical conditions. A representative set of parameters for pure niobium is provided to illustrate the model's structure and capabilities.

Together, these developments establish a physically-informed and extensible framework for modeling the plasticity of BCC metals, offering improved predictive accuracy and deeper insights into the role of dislocation character in deformation.

CHAPTER 5

CONCLUSIONS AND FUTURE WORK

This dissertation aims to advance the physical fidelity and practical calibration of crystal plasticity modeling for body-centered cubic (BCC) metals through a physics-informed approach. Spanning three major studies, this work bridges the investigation of parameter representativeness in model calibration, the full-range formulation of complex dislocation mobility, and the development of a comprehensive constitutive model that is both predictive and extensible.

Chapter 2 investigates the validity of surface-based measurements, such as those from surface slip trace analysis, for calibrating bulk crystal plasticity models. By systematically exploring the boundary sensitivity of stress responses, this study establishes when surface measurements are representative of the interior and when they fail. This work emphasizes the critical need for contextual awareness in experimental-model data pipelines and highlights how traditional calibration approaches can lead to biased or unreliable parameter extraction when surface effects appear.

Chapter 3 proposes a novel, generalized dislocation mobility law framework grounded in the kink-pair mechanism, which is one of the defining characteristics of plastic deformation in BCC metals. By avoiding restrictive assumptions common in earlier models, this framework captures the full range of dislocation velocities as a function of stress and temperature. Using principal component analysis (PCA), the study reduces complex atomistic data into a form amenable to continuum implementation, while preserving essential features of the underlying physics. This work enables more robust and transferable mobility laws across different material systems and thermomechanical conditions.

Chapter 4 develops a comprehensive constitutive model that explicitly accounts for both edge and screw dislocations in BCC metals. The model incorporates distinct mobility laws, accounting for the kink-pair-controlled motion of screw dislocations and the nearly athermal glide of edge dislocations. It also introduces dislocation density evolution laws for both monopoles and dipoles and incorporates key mechanisms such as cross-slip and climb. The model is implemented in

the DAMASK simulation platform, with switchable features to isolate and analyze the effects of individual mechanisms, such as non-Schmid behavior or cross-slip-enabled annihilation.

Together, these three works address core challenges in the crystal plasticity modeling of BCC metals:

- Calibration reliability: Establishing when and how surface-based experimental data can inform model parameters for bulk materials.
- Mobility accuracy: Developing transferable and physics-consistent mobility law framework for dislocation motion.
- Constitutive completeness: Building a constitutive model that accounts for character-specific behavior and microstructural evolution with high physical fidelity.

Planned future work includes:

- Calibration and validation of the constitutive law developed in Chapter 4, with experimental data extracted from the heat treatment of niobium sheets.
- Full-scale validation of the kink-pair-based mobility framework across various BCC alloys and other materials.
- Further investigation into how the initial distribution of dislocation content across slip systems influences the plastic response of metals.”

BIBLIOGRAPHY

- [1] Alankar Alankar, Philip Eisenlohr, and Dierk Raabe. A dislocation density-based crystal plasticity constitutive model for prismatic slip in α -titanium. *Acta Materialia*, 59(18):7003–7009, October 2011. doi:10.1016/j.actamat.2011.07.053.
- [2] Alankar Alankar, David P. Field, and Hussein M. Zbib. Explicit incorporation of cross-slip in a dislocation density-based crystal plasticity model. *Philosophical Magazine*, 92(24):3084–3100, August 2012. doi:10.1080/14786435.2012.685964.
- [3] A Arsenlis. On the evolution of crystallographic dislocation density in non-homogeneously deforming crystals. *Journal of the Mechanics and Physics of Solids*, 52(6):1213–1246, June 2004. doi:10.1016/j.jmps.2003.12.007.
- [4] Athanasios Arsenlis and David M. Parks. Modeling the evolution of crystallographic dislocation density in crystal plasticity. *Journal of the Mechanics and Physics of Solids*, 50(9):1979–2009, 2002.
- [5] Robert J. Asaro and JR0375 Rice. Strain localization in ductile single crystals. *Journal of the Mechanics and Physics of Solids*, 25(5):309–338, 1977.
- [6] A. Baczmański, P. Kot, S. Wroński, M. Wróbel, M. Wroński, J. Pilch, M. Muzyka, K. Wierzbanowski, Y. Zhao, L. Le Joncour, M. François, and B. Panicaud. Direct diffraction measurement of critical resolved shear stresses and stress localisation in magnesium alloy. *Materials Science and Engineering: A*, 801:140400, January 2021. doi:10.1016/j.msea.2020.140400.
- [7] A. Baczmański, M. Wroński, P. Kot, S. Wroński, A. Łabaza, K. Wierzbanowski, A. Ludwik, and M. Marciszko-Wiąckowska. The role of basal slip in the generation of intergranular stresses in magnesium alloy studied using X-ray diffraction and modelling. *Materials & Design*, 202:109543, April 2021. doi:10.1016/j.matdes.2021.109543.
- [8] G.H. Balbus, S.I. Rao, O.N. Senkov, and E.J. Payton. Orientation dependent plasticity of the refractory multi-principal element alloy MoNbTi investigated via micropillar compression. *Acta Materialia*, 262:119401, January 2024. doi:10.1016/j.actamat.2023.119401.
- [9] P. Berke, F. El Houdaigui, and T.J. Massart. Coupled friction and roughness surface effects in shallow spherical nanoindentation. *Wear*, 268(1-2):223–232, January 2010. doi:10.1016/j.wear.2009.07.015.
- [10] Cathy Bing, Thomas R. Bieler, and Philip Eisenlohr. A computational study of how surfaces affect slip family activity. *Acta Materialia*, 259:119246, October 2023. doi:10.1016/j.actamat.2023.119246.
- [11] W. Blum and P. Eisenlohr. Dislocation mechanics of creep. *Materials Science and Engi-*

- neering: A*, 510–511:7–13, June 2009. doi:10.1016/j.msea.2008.04.110.
- [12] M. S. Bobji and S. K. Biswas. Deconvolution of hardness from data obtained from nanoindentation of rough surfaces. *Journal of Materials Research*, 14(6):2259–2268, June 1999. doi:10.1557/JMR.1999.0302.
- [13] Max Boleininger, Martin Gallauer, Sergei L. Dudarev, Thomas D. Swinburne, Daniel R. Mason, and Danny Perez. Statistical mechanics of kinks on a gliding screw dislocation. *Physical Review Research*, 2(4):043254, November 2020. doi:10.1103/PhysRevResearch.2.043254.
- [14] N Brown and R.A Ekvall. Temperature dependence of the yield points in iron. *Acta Metallurgica*, 10(11):1101–1107, November 1962. doi:10.1016/0001-6160(62)90078-0.
- [15] S Brown, K Kim, and L Anand. An internal variable constitutive model for hot working of metals. *International Journal of Plasticity*, 5(2):95–130, 1989. doi:10.1016/0749-6419(89)90025-9.
- [16] Wei Cai, Vasily V Bulatov, Sidney Yip, and Ali S Argon. Kinetic Monte Carlo modeling of dislocation motion in BCC metals. *Materials Science and Engineering: A*, 309–310: 270–273, July 2001. doi:10.1016/S0921-5093(00)01689-0.
- [17] William D Callister and David G Rethwisch. *Materials Science and Engineering*.
- [18] David Cereceda, Martin Diehl, Franz Roters, Dierk Raabe, J. Manuel Perlado, and Jaime Marian. Unraveling the temperature dependence of the yield strength in single-crystal tungsten using atomistically-informed crystal plasticity calculations. *International Journal of Plasticity*, 78:242–265, March 2016. doi:10.1016/j.ijplas.2015.09.002.
- [19] Aritra Chakraborty, Chen Zhang, Shanoob Balachandran, Thomas R Bieler, and Philip Eisenlohr. Assessment of surface and bulk-dominated methodologies to measure critical resolved shear stresses in hexagonal materials.
- [20] Jinpeng Chang, Wei Cai, Vasily V Bulatov, and Sidney Yip. Molecular dynamics simulations of motion of edge and screw dislocations in a metal. *Computational Materials Science*, 23 (1-4):111–115, April 2002. doi:10.1016/S0927-0256(01)00221-X.
- [21] Bing Chen, Suzhi Li, Hongxiang Zong, Xiangdong Ding, Jun Sun, and Evan Ma. Unusual activated processes controlling dislocation motion in body-centered-cubic high-entropy alloys. *Proceedings of the National Academy of Sciences*, 117(28):16199–16206, July 2020. doi:10.1073/pnas.1919136117.
- [22] Martin Diehl, Pratheek Shanthraj, Philip Eisenlohr, and Franz Roters. Neighborhood influences on stress and strain partitioning in dual-phase microstructures: An investigation on synthetic polycrystals with a robust spectral-based numerical method. *Meccanica*, 51(2): 429–441, February 2016. doi:10.1007/s11012-015-0281-2.

- [23] John E. Dora and Stanley Rajnak. Nucleation of Kink Pairs and the Peierls' Mechanism of Plastic Deformation. *Gordon Research Conference*, July 1963.
- [24] M S Duesbery and V Vitek. PLASTIC ANISOTROPY IN B.C.C. TRANSITION METALS. 1997.
- [25] Keiichi Edagawa, Takayoshi Suzuki, and Shin Takeuchi. Motion of a screw dislocation in a two-dimensional Peierls potential. *Physical Review B*, 55(10):6180–6187, March 1997. doi:10.1103/PhysRevB.55.6180.
- [26] Philip Eisenlohr. On the role of dislocation dipoles in unidirectional deformation of crystals.
- [27] Lauren T. W. Fey, Abigail Hunter, and Irene J. Beyerlein. Phase-field dislocation modeling of cross-slip. *Journal of Materials Science*, 57(23):10585–10599, June 2022. doi:10.1007/s10853-021-06716-1.
- [28] S. P. Fitzgerald. Kink pair production and dislocation motion. *Scientific Reports*, 6(1):39708, December 2016. doi:10.1038/srep39708.
- [29] R. A. Foxall and C. D. Statham. Dislocation arrangements in deformed single crystals of niobium-molybdenum alloys and niobium-9 at.% rhenium. *Acta Metallurgica*, 18(11):1147–1158, 1970.
- [30] J. Frenkel. Zur Theorie der Elastizitätsgrenze und der Festigkeit kristallinischer Körper. *Zeitschrift für Physik*, 37(7-8):572–609, July 1926. doi:10.1007/BF01397292.
- [31] John Price Hirth and Jens Lothe. *Theory of Dislocations*. A Wiley-Interscience Publication. Wiley, New York, NY, 2. ed edition, 1982. ISBN 978-0-471-09125-7.
- [32] K. Ito and V. Vitek. Atomistic study of non-Schmid effects in the plastic yielding of bcc metals. *Philosophical Magazine A*, 81(5):1387–1407, May 2001. doi:10.1080/01418610108214447.
- [33] M.R. Jones, L.T.W. Fey, and I.J. Beyerlein. Phase-field dislocation dynamics simulations of temperature-dependent glide mechanisms in niobium. *Computational Materials Science*, 232:112652, January 2024. doi:10.1016/j.commatsci.2023.112652.
- [34] U. F. Kocks. Thermodynamics and Kinetics of Slip.
- [35] Aenne Koester, Anxin Ma, and Alexander Hartmaier. Atomistically informed crystal plasticity model for body-centered cubic iron. *Acta Materialia*, 60(9):3894–3901, May 2012. doi:10.1016/j.actamat.2012.03.053.
- [36] L. Kubin. *Dislocations, Mesoscale Simulations and Plastic Flow*. OUP Oxford, April 2013. ISBN 978-0-19-852501-1.

- [37] Ladislav P. Kubin, G. Canova, M. Condat, Benoit Devincre, V. Pontikis, and Yves Bréchet. Dislocation Microstructures and Plastic Flow: A 3D Simulation. *Solid State Phenomena*, 23–24:455–472, January 1992. doi:10.4028/www.scientific.net/SSP.23-24.455.
- [38] H. Li, D.E. Mason, T.R. Bieler, C.J. Boehlert, and M.A. Crimp. Methodology for estimating the critical resolved shear stress ratios of α -phase Ti using EBSD-based trace analysis. *Acta Materialia*, 61(20):7555–7567, December 2013. doi:10.1016/j.actamat.2013.08.042.
- [39] Y. Liu, S. Varghese, J. Ma, M. Yoshino, H. Lu, and R. Komanduri. Orientation effects in nanoindentation of single crystal copper. *International Journal of Plasticity*, 24(11):1990–2015, November 2008. doi:10.1016/j.ijplas.2008.02.009.
- [40] Jens Lothe. Theory of Dislocation Mobility in Pure Slip. *Journal of Applied Physics*, 33(6):2116–2125, June 1962. doi:10.1063/1.1728907.
- [41] F. Louchet, L. P. Kubin, and D. Vesely. In situ deformation of b.c.c. crystals at low temperatures in a high-voltage electron microscope Dislocation mechanisms and strain-rate equation. *Philosophical Magazine A*, 39(4):433–454, April 1979. doi:10.1080/01418617908239283.
- [42] Yan Lu, Yu-Heng Zhang, En Ma, and Wei-Zhong Han. Relative mobility of screw versus edge dislocations controls the ductile-to-brittle transition in metals. *Proceedings of the National Academy of Sciences*, 118(37):e2110596118, September 2021. doi:10.1073/pnas.2110596118.
- [43] A. Ma and F. Roters. A constitutive model for fcc single crystals based on dislocation densities and its application to uniaxial compression of aluminium single crystals. *Acta Materialia*, 52(12):3603–3612, July 2004. doi:10.1016/j.actamat.2004.04.012.
- [44] Ronan Madec and Ladislav P. Kubin. Dislocation strengthening in FCC metals and in BCC metals at high temperatures. *Acta Materialia*, 126:166–173, March 2017. doi:10.1016/j.actamat.2016.12.040.
- [45] Tias Maiti and Philip Eisenlohr. Fourier-based spectral method solution to finite strain crystal plasticity with free surfaces. *Scripta Materialia*, 145:37–40, March 2018. doi:10.1016/j.scriptamat.2017.09.047.
- [46] Jaime Marian, Wei Cai, and Vasily V. Bulatov. Dynamic transitions from smooth to rough to twinning in dislocation motion. *Nature Materials*, 3(3):158–163, March 2004. doi:10.1038/nmat1072.
- [47] G. Monnet and D. Terentyev. Structure and mobility of the $12\{112\}$ edge dislocation in BCC iron studied by molecular dynamics. *Acta Materialia*, 57(5):1416–1426, March 2009. doi:10.1016/j.actamat.2008.11.030.
- [48] Ghiath Monnet, Ludovic Vincent, and Benoit Devincre. Dislocation-dynamics based crystal

- plasticity law for the low- and high-temperature deformation regimes of bcc crystal. *Acta Materialia*, 61(16):6178–6190, September 2013. doi:10.1016/j.actamat.2013.07.002.
- [49] S. Naamane, G. Monnet, and B. Devincere. Low temperature deformation in iron studied with dislocation dynamics simulations. *International Journal of Plasticity*, 26(1):84–92, January 2010. doi:10.1016/j.ijplas.2009.05.003.
- [50] Supriya Nandy, Shao-Pu Tsai, Leigh Stephenson, Dierk Raabe, and Stefan Zaeferrer. The role of Ca, Al and Zn on room temperature ductility and grain boundary cohesion of magnesium. *Journal of Magnesium and Alloys*, 9(5):1521–1536, September 2021. doi:10.1016/j.jma.2021.03.005.
- [51] Sia Nemat-Nasser, Tomoo Okinaka, and Luqun Ni. A physically-based constitutive model for bcc crystals with application to polycrystalline tantalum. *Journal of the Mechanics and Physics of Solids*, 46(6):1009–1038, June 1998. doi:10.1016/S0022-5096(97)00064-1.
- [52] Pham T. N. Nguyen, Fazilay Abbès, Jean-Sébastien Lecomte, Christophe Schuman, and Boussad Abbès. Inverse Identification of Single-Crystal Plasticity Parameters of HCP Zinc from Nanoindentation Curves and Residual Topographies. *Nanomaterials*, 12(3):300, January 2022. doi:10.3390/nano12030300.
- [53] E. Orowan. Zur Kristallplastizität. I. *Zeitschrift für Physik*, 89(9):605–613, September 1934. doi:10.1007/BF01341478.
- [54] Darren C. Pagan, Joel V. Bernier, Darren Dale, J.Y. Peter Ko, Todd J. Turner, Basil Blank, and Paul A. Shade. Measuring Ti-7Al slip system strengths at elevated temperature using high-energy X-ray diffraction. *Scripta Materialia*, 142:96–100, January 2018. doi:10.1016/j.scriptamat.2017.08.029.
- [55] Darren C. Pagan, Kelly E. Nygren, and Matthew P. Miller. Analysis of a three-dimensional slip field in a hexagonal Ti alloy from in-situ high-energy X-ray diffraction microscopy data. *Acta Materialia*, 221:117372, December 2021. doi:10.1016/j.actamat.2021.117372.
- [56] Pai Kulyadi, Eureka. *Investigating Single Crystal Plasticity of Niobium with a Dislocation Mechanics-Based Model*. PhD thesis, Michigan State University.
- [57] Anirban Patra and David L. McDowell. Crystal plasticity-based constitutive modelling of irradiated bcc structures. *Philosophical Magazine*, 92(7):861–887, March 2012. doi:10.1080/14786435.2011.634855.
- [58] R Peierls. The size of a dislocation. *Proceedings of the Physical Society*, 52(1):34–37, January 1940. doi:10.1088/0959-5309/52/1/305.
- [59] D. Peirce, R.J. Asaro, and A. Needleman. An analysis of nonuniform and localized deformation in ductile single crystals. *Acta Metallurgica*, 30(6):1087–1119, June 1982.

doi:10.1016/0001-6160(82)90005-0.

- [60] Giacomo Po, Yinan Cui, David Rivera, David Cereceda, Tom D. Swinburne, Jaime Marian, and Nasr Ghoniem. A phenomenological dislocation mobility law for bcc metals. *Acta Materialia*, 119:123–135, October 2016. doi:10.1016/j.actamat.2016.08.016.
- [61] Reemu Pokharel, Jonathan Lind, Anand K. Kanjarla, Ricardo A. Lebensohn, Shiu Fai Li, Peter Kenesei, Robert M. Suter, and Anthony D. Rollett. Polycrystal Plasticity: Comparison Between Grain - Scale Observations of Deformation and Simulations. *Annual Review of Condensed Matter Physics*, 5(1):317–346, March 2014. doi:10.1146/annurev-conmatphys-031113-133846.
- [62] M. Polanyi. Über eine Art Gitterstörung, die einen Kristall plastisch machen könnte. *Zeitschrift für Physik*, 89:660–664, September 1934. doi:10.1007/BF01341481.
- [63] S. Queyreau, J. Marian, M. R. Gilbert, and B. D. Wirth. Edge dislocation mobilities in bcc Fe obtained by molecular dynamics. *Physical Review B*, 84(6):064106, August 2011. doi:10.1103/PhysRevB.84.064106.
- [64] Sylvain Queyreau, Ghiath Monnet, and Benoît Devincere. Slip systems interactions in α -iron determined by dislocation dynamics simulations. *International Journal of Plasticity*, 25(2): 361–377, February 2009. doi:10.1016/j.ijplas.2007.12.009.
- [65] M Rhee, H M Zbib, J P Hirth, H Huang, and T De La Rubia. Models for long-/short-range interactions and cross slip in 3D dislocation simulation of BCC single crystals. *Modelling and Simulation in Materials Science and Engineering*, 6(4):467–492, July 1998. doi:10.1088/0965-0393/6/4/012.
- [66] James R. Rice. Inelastic constitutive relations for solids: An internal-variable theory and its application to metal plasticity. *Journal of the Mechanics and Physics of Solids*, 19(6): 433–455, 1971.
- [67] F. Roters, P. Eisenlohr, L. Hantcherli, D.D. Tjahjanto, T.R. Bieler, and D. Raabe. Overview of constitutive laws, kinematics, homogenization and multiscale methods in crystal plasticity finite-element modeling: Theory, experiments, applications. *Acta Materialia*, 58(4):1152–1211, February 2010. doi:10.1016/j.actamat.2009.10.058.
- [68] F. Roters, M. Diehl, P. Shanthraj, P. Eisenlohr, C. Reuber, S.L. Wong, T. Maiti, A. Ebrahimi, T. Hochrainer, H.-O. Fabritius, S. Nikolov, M. Friák, N. Fujita, N. Grilli, K.G.F. Janssens, N. Jia, P.J.J. Kok, D. Ma, F. Meier, E. Werner, M. Stricker, D. Weygand, and D. Raabe. DAMASK – The Düsseldorf Advanced Material Simulation Kit for modeling multi-physics crystal plasticity, thermal, and damage phenomena from the single crystal up to the component scale. *Computational Materials Science*, 158:420–478, February 2019. doi:10.1016/j.commatsci.2018.04.030.

- [69] Franz Roters, Philip Eisenlohr, Thomas R. Bieler, and Dierk Raabe. *Crystal Plasticity Finite Element Methods: In Materials Science and Engineering*. Wiley, 1 edition, October 2010. ISBN 978-3-527-32447-7 978-3-527-63148-3. doi:10.1002/9783527631483.
- [70] G. Sachs. Zur ableitung einer fließbedingung. *Z. Ver, Dtsch. Ing.*, 72:734–736, 1928.
- [71] R. Sánchez-Martín, M.T. Pérez-Prado, J. Segurado, J. Bohlen, I. Gutiérrez-Urrutia, J. Llorca, and J.M. Molina-Aldareguia. Measuring the critical resolved shear stresses in Mg alloys by instrumented nanoindentation. *Acta Materialia*, 71:283–292, June 2014. doi:10.1016/j.actamat.2014.03.014.
- [72] Siegfried Schmauder, Chuin-Shan Chen, Krishan K. Chawla, Nikhilesh Chawla, Weiqiu Chen, and Yutaka Kagawa, editors. *Handbook of Mechanics of Materials*. Springer Singapore, Singapore, 2019. ISBN 978-981-10-6883-6 978-981-10-6884-3. doi:10.1007/978-981-10-6884-3.
- [73] Erich Schmid and Walter Boas. *Plasticity of crystals*. 1950.
- [74] K. Sedighiani, M. Diehl, K. Traka, F. Roters, J. Sietsma, and D. Raabe. An efficient and robust approach to determine material parameters of crystal plasticity constitutive laws from macro-scale stress–strain curves. *International Journal of Plasticity*, 134:102779, November 2020. doi:10.1016/j.ijplas.2020.102779.
- [75] A. Seeger. The Flow Stress of High-Purity Refractory Body-Centred Cubic Metals and its Modification by Atomic Defects. *Le Journal de Physique IV*, 05(C7):C7–45–C7–65, November 1995. doi:10.1051/jp4:1995704.
- [76] Alfred Seeger. Peierls barriers, kinks, and flow stress: Recent progress: Dedicated to Professor Dr. Haël Mughrabi on the occasion of his 65th birthday. *Zeitschrift für Metallkunde*, 93(8):760–777, August 2002. doi:10.3139/146.020760.
- [77] Alfred Seeger. Progress and problems in the understanding of the dislocation relaxation processes in metals. *Materials Science and Engineering: A*, 370(1-2):50–66, 2004.
- [78] P. Shanthraj, P. Eisenlohr, M. Diehl, and F. Roters. Numerically robust spectral methods for crystal plasticity simulations of heterogeneous materials. *International Journal of Plasticity*, 66:31–45, March 2015. doi:10.1016/j.ijplas.2014.02.006.
- [79] P. Shanthraj, B. Svendsen, L. Sharma, F. Roters, and D. Raabe. Elasto-viscoplastic phase field modelling of anisotropic cleavage fracture. *Journal of the Mechanics and Physics of Solids*, 99:19–34, February 2017. doi:10.1016/j.jmps.2016.10.012.
- [80] T. D. Swinburne and S. L. Dudarev. Kink-limited Orowan strengthening explains the brittle to ductile transition of irradiated and unirradiated bcc metals. *Physical Review Materials*, 2(7):073608, July 2018. doi:10.1103/PhysRevMaterials.2.073608.

- [81] T. D. Swinburne, S. L. Dudarev, and A. P. Sutton. Classical Mobility of Highly Mobile Crystal Defects. *Physical Review Letters*, 113(21):215501, November 2014. doi:10.1103/PhysRevLett.113.215501.
- [82] Y. Talmor, E. Walker, P. A. Maesli, and S. Steinemann. Elastic constants of Nb-Zr single crystal alloys between 4.2 K and the melting point. *Helv. Phys. Acta;(Switzerland)*, 50(5), 1977.
- [83] M. Tang, L. P. Kubin, and G. R. Canova. Dislocation mobility and the mechanical response of b.c.c. single crystals: A mesoscopic approach. *Acta Materialia*, 46(9):3221–3235, May 1998. doi:10.1016/S1359-6454(98)00006-8.
- [84] G. I. Taylor. The mechanism of plastic deformation of crystals. Part I.—Theoretical. *Proceedings of the Royal Society of London. Series A, Containing Papers of a Mathematical and Physical Character*, 145(855):362–387, July 1934. doi:10.1098/rspa.1934.0106.
- [85] Geoffrey Ingram Taylor. Plastic strain in metals. *J. Inst. Metals*, 62:307–324, 1938.
- [86] C. Tomé and U. F. Kocks. The yield surface of h.c.p. crystals. *Acta Metallurgica*, 33(4): 603–621, April 1985. doi:10.1016/0001-6160(85)90025-2.
- [87] V. Vitek. Core structure of screw dislocations in body-centred cubic metals: Relation to symmetry and interatomic bonding. *Philosophical Magazine*, 84(3-5):415–428, January 2004. doi:10.1080/14786430310001611644.
- [88] V. Vitek and M. Yamaguchi. Core structure of nonscrew $1/2(111)$ dislocations on (110) planes in b.c.c. crystals. II. Peierls stress and the effect of an external shear stress on the cores. *Journal of Physics F: Metal Physics*, 3(3):537, March 1973. doi:10.1088/0305-4608/3/3/011.
- [89] Vignesh Vivekanandan, Peng Lin, Grethe Winther, and Anter El-Azab. On the implementation of dislocation reactions in continuum dislocation dynamics modeling of mesoscale plasticity. *Journal of the Mechanics and Physics of Solids*, 149:104327, April 2021. doi:10.1016/j.jmps.2021.104327.
- [90] L. Wang, Z. Zheng, H. Phukan, P. Kenesei, J.-S. Park, J. Lind, R.M. Suter, and T.R. Bieler. Direct measurement of critical resolved shear stress of prismatic and basal slip in polycrystalline Ti using high energy X-ray diffraction microscopy. *Acta Materialia*, 132: 598–610, June 2017. doi:10.1016/j.actamat.2017.05.015.
- [91] Leyun Wang, Zhonghe Huang, Huamiao Wang, Alireza Maldar, Sangbong Yi, Jun-Sang Park, Peter Kenesei, Erica Lilleodden, and Xiaoqin Zeng. Study of slip activity in a Mg-Y alloy by in situ high energy X-ray diffraction microscopy and elastic viscoplastic self-consistent modeling. *Acta Materialia*, 155:138–152, August 2018. doi:10.1016/j.actamat.2018.05.065.

- [92] C R Weinberger, B L Boyce, and C C Battaile. Slip planes in bcc transition metals. *International Materials Reviews*, 58(5):296–314, June 2013. doi:10.1179/1743280412Y.0000000015.
- [93] Christopher R. Weinberger, Garritt J. Tucker, and Stephen M. Foiles. Peierls potential of screw dislocations in bcc transition metals: Predictions from density functional theory. *Physical Review B*, 87(5):054114, February 2013. doi:10.1103/PhysRevB.87.054114.
- [94] J C Williams, R G Baggerly, and N E Paton. Deformation behavior of HCP Ti-Al alloy single crystals.
- [95] Shuozhi Xu, Wu-Rong Jian, Yanqing Su, and Irene J. Beyerlein. Line-length-dependent dislocation glide in refractory multi-principal element alloys. *Applied Physics Letters*, 120(6):061901, February 2022. doi:10.1063/5.0080849.
- [96] L.H Yang and J.A Moriarty. Kink-pair mechanisms for $a/2 \langle 111 \rangle$ screw dislocation motion in bcc tantalum. *Materials Science and Engineering: A*, 319–321:124–129, December 2001. doi:10.1016/S0921-5093(01)01020-6.
- [97] Song Yu, Chong-Yu Wang, and Tao Yu. The kink-pair nucleation in edge dislocation motion. *Solid State Sciences*, 11(3):733–739, March 2009. doi:10.1016/j.solidstatesciences.2008.08.005.
- [98] Claudio Zambaldi, Yiyi Yang, Thomas R. Bieler, and Dierk Raabe. Orientation informed nanoindentation of α -titanium: Indentation pileup in hexagonal metals deforming by prismatic slip. *Journal of Materials Research*, 27(1):356–367, January 2012. doi:10.1557/jmr.2011.334.
- [99] Z. Zhao, W. Mao, F. Roters, and D. Raabe. A texture optimization study for minimum earing in aluminium by use of a texture component crystal plasticity finite element method. *Acta Materialia*, 52(4):1003–1012, February 2004. doi:10.1016/j.actamat.2003.03.001.
- [100] Z. Zhao, M. R. Ruiz, J. Lu, M. A. Monclús, J. M. Molina-Aldareguía, T. R. Bieler, and P. Eisenlohr. Quantifying the Uncertainty of Critical Resolved Shear Stress Values Derived from Nano-Indentation in Hexagonal Ti Alloys. *Experimental Mechanics*, 62(5):731–743, June 2022. doi:10.1007/s11340-021-00813-7.
- [101] Xinran Zhou and Jaime Marian. Temperature and Stress Dependence of Screw Dislocation Mobility in Nb-V-Ta Alloys Using Kinetic Monte Carlo Simulations. *Frontiers in Materials*, 8:801141, December 2021. doi:10.3389/fmats.2021.801141.
- [102] Olgierd Cecil Zienkiewicz and Robert Leroy Taylor. *The Finite Element Method for Solid and Structural Mechanics*. Elsevier, 2005.